THE ASTROPHYSICAL JOURNAL SUPPLEMENT SERIES, 103:63–79, 1996 March

THE PEAK-PATCH PICTURE OF COSMIC CATALOGS. III. APPLICATION TO CLUSTERS

J. R. BOND
CIAR Cosmology Program, Canadian Institute for Theoretical Astrophysics McLennan Physical Laboratories, Toronto, Ont. M5S 1A1, Canada
AND
S. T. MYERS
Department of Astronomy, 105-24, Caltech, Pasadena CA 91125; David Rittenhouse Laboratory, University of Pennsylvania, 209 S. 33d Street, Philadelphia, PA 19104-6396
Received 1993 August 2; accepted 1995 June 16

ABSTRACT

In adjoining papers, we developed a picture of large-scale structure formation based upon the collapse and flow of regions of Lagrangian (initial condition) space surrounding peaks in the density field. To illustrate the utility of this "Peak-Patch" method, we construct cluster catalogues covering very large volumes of space for four inflation-inspired Gaussian structure formation theories with a critical density in clustering matter and whose σ_8 normalizations roughly fit the *COBE* anisotropy measurements. We use these to make deep field X-ray and Sunyaev-Zeldovich maps. Subject to some uncertainties in the internal peak-patch physics and the X-ray data, we find that current X-ray temperature data suggest σ_8 is within $\sim$15% of 0.7 and the spectrum is flatter than CDM gives, for Einstein–de Sitter models. We also find the current X-ray luminosity data are difficult to fit over the entire range with such models. The prospect for the observation of the ambient thermal and kinetic SZ effect with a variety of experimental designs is discussed.

Subject headings: catalogs — cosmology: theory — galaxies: clusters: general — methods: numerical

1. INTRODUCTION

In a series of papers (Bond & Myers 1995a, b, c, hereafter BM1, BM2, BM4), we have presented the hierarchical peak-patch picture as a way to generate point processes associated with deep gravitational potential wells, which is more physically correct than the original single-filter snapshot of density peaks (Bardeen et al. 1986, hereafter BBKS), and which matches the results of N-body simulations (BM2). The ultimate aim of the peak-patch method is to set down a language for discussion of structure formation from the point of view of collapsing regions of Lagrangian space. From this, we can obtain the cosmic mass and velocity functions, spatial distribution, and redshift evolution of the astronomical objects associated with the gravitational wells generated by the algorithm. The peak-patch algorithm itself was described in BM1, the analytic and semi-analytic calculational methods will be presented in BM4, and the validation of the method through detailed comparison with an N-body simulation was presented in BM2. In this paper (referred to in the other papers as BM3), we use the peak patch method to generate catalogs of clusters of galaxies under different cosmological models and through comparison with observations evaluate the efficacy of these models in reproducing the structure we see around us in the universe.

What we find frustrating about the current state of our cosmological theorizing, however, is that the mapping from our computed internal peak-patch properties to cluster observables such as galaxy velocity dispersions and X-ray temperatures and luminosities must be parameterized by "fudge" factors of order unity. To fix these one will need a suite of full local hydrodynamical/N-body simulations of a well chosen subset of peak patches and the immediate environment around them. Many of the parameters must now be set not by what we know the theoretical model predicts, but rather by what the theory would need to give if it were to match observations of real clusters—looking at the answer in the back of the book, so to speak. A case in point is the core radius of clusters. We parameterize some of the uncertainties in internal cluster physics in § 3.

If the standard CDM model with a Harrison-Zeldovich initial spectrum of density fluctuations ($n_s = 1$) is normalized to the fluctuation level inferred by *COBE*'s DMR experiment (Smoot et al. 1992), one gets $\sigma_8 \approx 1.3$ (Bond 1995). It is well known that if fluctuations in the galaxy number density on large scales are just linear amplifications of the fluctuations in the dark matter density, then the standard CDM model fails to reproduce the shape of the angular correlation function of galaxies. Since the mid 1980s, when the large-scale structure problems began to emerge, many theories with enhanced large-scale power in the density fluctuations have been explored (e.g., Bardeen, Bond, & Efstathiou 1987). We compare results for the standard CDM model with three other nearly scale-invariant and *COBE* normalized models having enhanced power and motivated by the inflationary paradigm, with $h = 0.5$ and $\Omega_{\rm nr} = 1$, where $\Omega_{\rm nr}$ is the density parameter in nonrelativistic (i.e., clustering) particles. These four models show the dramatic effects of changing σ_8 by a factor of 2, and the effects of flattening the spectrum in the cluster range. We calculate all sky catalogues to $z = 0.1$ to compare with X-ray data in § 4 and deep catalogs to $z = 1.5$ (§ 2.) which we use to construct *ROSAT* and Sunyaev-Zeldovich maps (§ 5).

It has long been recognized that the abundances of clusters can be used to constrain the "biasing factor" $b_8 = 1/\sigma_8$ of the linear density fluctuation spectrum: using rough cluster information, with peak methods (e.g., BBKS; Bardeen et al. 1987; Bond 1988, 1989, Peebles, Daly, & Juszkiewicz 1989; Adams et al. 1993), or with Press-Schechter methods (e.g., Cole &

Kaiser 1988); or using more detailed optical velocity dispersion or X-ray information, for the hierarchical peak method (Bond & Myers 1991, 1993b) or with Press-Schechter methods (e.g., Evrard 1990b; Kaiser 1991; Evrard & Henry 1991; Henry & Arnaud 1991; Blanchard et al. 1992; Bartlett & Silk 1993; Oukbir & Blanchard 1992). However, it has always been unclear how accurate the theoretical estimates of the mass and velocity dispersion functions of rare clusters were. Scattered among the many papers that rely on the few checks of the Press-Schechter mass function that have been made (e.g., by Efstathiou et al. 1988; Narayan & White 1987; Efstathiou & Rees 1988; Carlberg & Couchman 1989; Bond et al. 1991) are a few papers that directly use N-body or gasdynamical simulations to determine the distribution of cluster properties (e.g., Frenk et al. 1990, Cen & Ostriker 1992; Bahcall & Cen 1993; White, Efstathiou, & Frenk 1992). In BM2, we tested the accuracy of the peak-patch technique and showed it was quite acceptable. Here we apply it to the estimation of σ_8, based on current X-ray data.

2. SIMULATIONS OF DEEP GROUP AND CLUSTER CATALOGS

The BM2 success in reproducing the locations and gross properties of N-body clusters gives confidence in the method, especially for the rarest clusters. Although doing all of the Fourier transforms and merging the peaks carries some computational cost, the gain in speed over adaptive P^3M calculations is many hundred-fold. Now we turn to a sample set of simulations that will illustrate the true power of the method, a calculation that would be quite difficult to do currently with N-body codes, even by PM calculations with the very large grids that have recently become feasible.

For this demonstration, we construct a cluster and group catalogue by laying down an inverted pyramid of 200 h^{-1} Mpc boxes which contain within it a 5° cone, as described in BM1. The boxes go out to a distance beyond which there are very few groups of the masses of interest. We take the cutoff here to be redshift $z = 1.5$, corresponding to a distance of 2200 h^{-1} Mpc for our assumed models.

2.1. *Theoretical Models*

For the illustrations, we shall simulate and compare four inflation-inspired theoretical models of cosmic structure formation. We shall assume a universe in which $\Omega = 1$, and the density in nonrelativistic (clustering) matter, $\Omega_{\rm nr}$, is also unity; i.e., we set both the mean curvature and the cosmological constant to zero. We also take $h = 0.5$ to ensure that the universe is old enough (13 Gyr) to (possibly) accommodate the oldest stars in these $\Omega_{\rm nr} = 1$ models. The initial density fluctuations are assumed to be Gaussian and adiabatic, with a power spectrum characterized by an initial spectral index n_s. For all but one of the models, we take n_s to be unity, the Harrison-Zeldovich spectral index, and for the one that is not, we take a nearly scale-invariant spectrum, with a slight tilt to give more power on large scales, $n_s = 0.8$. Spectral indices n_s with much more tilt or which vary with wavenumber over the (relatively narrow) observable range are rather difficult to generate by quantum noise in the inflation field (e.g., Bardeen, Steinhardt, & Turner 1983; Salopek, Bond, & Bardeen 1989).

The level of dynamical clustering is usually parameterized by the size of the mass fluctuations in 8 h^{-1} Mpc spheres, σ_8. The abundance of massive clusters as a function of redshift is a sensitive probe of the amplitude of the density fluctuations on the scale $k^{-1} \sim (3\text{–}8)\,h^{-1}$ Mpc, hence of σ_8. We choose σ_8 so that the very large scale gravitational potential fluctuations ($k^{-1} \sim 300\text{–}6000\,h^{-1}$ Mpc) are in rough agreement with the value one can estimate from the *COBE* detection if the source of the *COBE* anisotropies is the Sachs-Wolfe effect.

Figure 1 shows "wedge" diagrams for clusters with virialized ("internal binding energy") velocities $v_{E,\rm pk} > 850$ km s^{-1} found in the hierarchical peak-patch catalogs of the four models we simulate, for 5° × 5° areas of sky projected back to $z = 1.5$. The y-axis comoving positions are projected onto the comoving x-z plane. The relative abundances of high-mass compared with low-mass clusters depends upon the detailed shape of the spectrum, and this differs for each of the models. However, by far the defining characteristic is the remarkable sensitivity of the number of clusters to the value of σ_8, which varies by only a factor of 2 over the four diagrams.

The first of the four models we simulate, A, is the $\sigma_8 = 1$ standard CDM model with $n_s = 1$. This is essentially the model we have used in BM2 to "validate" our method, (actually, we used $\sigma_8 = 0.97$). A scale-invariant ($n_s = 1$) CDM model with a

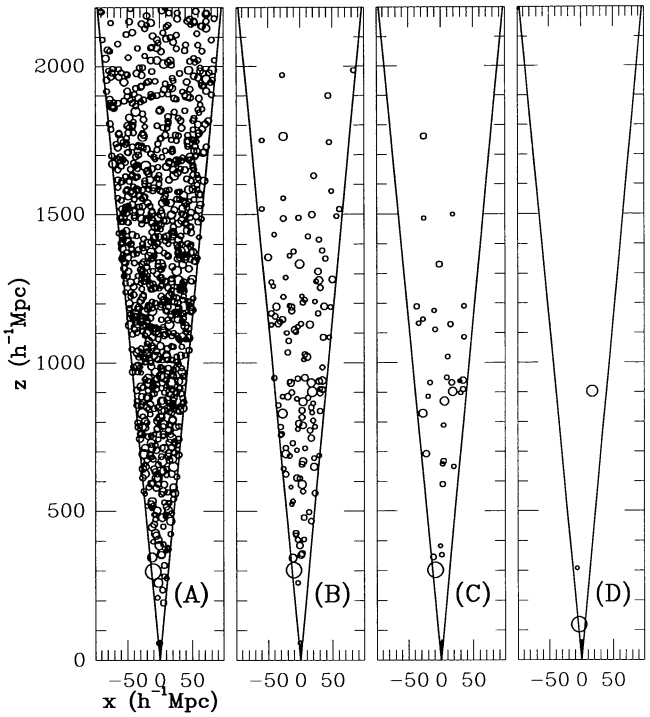

FIG. 1.—"Wedge" diagrams give the comoving (x, z) positions of clusters with virialized velocities $v_{E,\rm pk} > 850$ km s^{-1}, for 5° × 5° areas of sky out to redshift 1.5. Redshifts 0.3, 0.5, 0.7, and 1 are at distances 740, 1100, 1400, and 1760 h^{-1} Mpc. The circle drawn about the cluster has radius $\propto M_{\rm pk}^{1/3}$. Four models using the same initial random seeds are shown: (A) $\sigma_8 = 1$ standard CDM, with $n_s = 1$; (B) $\sigma_8 = 0.71$ tilted CDM model, with $n_s = 0.8$; (C) $\sigma_8 = 0.71$ HDM-CDM hybrid, with $\Omega_\nu = 0.3$; (D) $\sigma_8 = 0.45$ CDM with $\Gamma = 0.2$ (e.g., from a keV ν_τ with a 17 year life). The σ_8's are normalized to fit the *COBE* anisotropies. Models C and D fit the galaxy clustering data.

baryon density parameter $\Omega_B = 0.05$ normalized to the two-year *COBE* data has $\sigma_8 = 1.34 \pm 0.11$ (Bond 1995). Thus $\sigma_8 = 1$ is low. In the most conventional models of inflation there is usually a slight tilt (e.g., $n_s \approx 0.95$ for chaotic inflation). Although this does not alter by much the shape of the power spectrum over the waveband range important for clusters, it does lead to a $e^{2.63}(n_s - 1)$ decrease in σ_8, as normalized by *COBE*. It is also generically expected in such inflation models that some of *COBE*'s signal will be the imprint of primordial gravitational waves generated during inflation, and this would typically lead to a further $[1 - 6(n_s - 1)]^{-1/2}$ decrease.

The other three $\Omega_{nr} = 1$ models are designed to have more large-scale power than the standard $n_s = 1$ CDM model. The first increases the tilt a bit more, to $n_s = 0.8$. This has a dramatic effect on σ_8, dropping it by 40% for models with no gravity wave imprint ($\sigma_8 \approx 0.79 \pm 0.07$), and by 60% for models with gravity waves ($\sigma_8 \approx 0.51 \pm 0.04$). See, e.g., Adams et al. (1993) and Bond (1995). We choose to simulate a $\sigma_8 \approx 0.7$ model B. As we shall see, models with $\sigma_8 \lesssim 0.5$ are very cluster poor. The shape of the CDM power spectrum with $n_s = 0.8$ is actually not tilted enough to explain the current observations of large-scale clustering, especially the angular correlation function derived from the APM and other surveys. One needs $0 \lesssim n_s \lesssim 0.6$ (e.g., Adams et al. 1993). However, even with no gravity wave imprint, $\sigma_8 \lesssim 0.5$ is needed for the $n_s = 0.6$ model to agree with *COBE* and σ_8 is hopelessly too small for models with typical gravity wave contributions.

Models which look reasonably promising to explain the current large-scale structure data are those that have some hot dark matter (light massive neutrinos with density Ω_ν) as well as a dominant cold component (with Ω_{cdm} plus Ω_B making up the rest of the contribution to $\Omega_{nr} = 1$). The neutrinos are sufficiently cool by $z = 1.5$ that they are effectively a cold component as far as the clustering on cluster scales is concerned. These hot/cold hybrid models or mixed dark matter models cannot have too large a value of Ω_ν (i.e., of the neutrino mass) or the epoch of galaxy formation would be too late (Bardeen et al. 1987). However, it appears that the galaxy formation epoch may not be a problem if Ω_ν is in the range $\sim$0.1–0.3. There is enough extra large-scale power compared with the $\Omega_{cdm} = 1$ model that the angular correlation function of galaxies can be explained (Bardeen et al. 1987; van Dalen & Schaeffer 1992; Davis, Summers, & Schlegel 1992; Klypin et al. 1993). We denote the hybrid model with $\Omega_\nu = 0.3$ corresponding to a neutrino mass of 7 eV by (C) in the figures. A van Dalen & Schaeffer (1992) transfer function was used. The amplitude used is $\sigma_8 \approx 0.7$. The amplitude for $n_s = 1$ from *COBE* is 1.08 $\pm$ .09, but with a $n_s = 0.95$ tilt and a standard gravity wave contribution, it is $\sigma_8 \simeq 0.83 \pm 0.07$.

Model D is an example from a class of models with extra large-scale power which are parameterized by a factor Γ (Efstathiou, Bond, & White 1992). The standard CDM models have $\Gamma \approx 0.5$, and the range that is required to explain the large-scale clustering data is $\Gamma \approx 0.15$–0.3. Model D has $\Gamma = 0.2$ and $n_s = 1$. Models with nonzero cosmological constant or open models have $\Gamma \approx \Omega_{nr}h$. Here we consider instead an $\Omega_{nr} = 1$ model with this value of Γ, one with a decaying neutrino (e.g., the tau neutrino) as well as CDM and baryons with densities satisfying $\Omega_{cdm} + \Omega_B = 1$. To get $\Gamma = 0.2$, the following relationship between mass m_ν and decay lifetime τ_d must hold: $\tau_d = (16.5 \text{ keV}/m_\nu)$ yr (Bond & Efstathiou 1991). The amplitude derived from *COBE* is $\sigma_8 \approx 0.51 \pm 0.04$. We chose 0.45 for the figures.

2.2. *Evolution across Simulation Volumes*

The three-dimensional velocity cut, 850 km s^{-1} (i.e., a one-dimensional cut at 500 km s^{-1}), was chosen to ensure that there would be at least one cluster in the $\sigma_8 = 0.45$ model (D). These figures show dramatically that, with well determined internal energies of virialized clusters as a function of redshift, we have a very powerful probe of σ_8. The influence of the shape of the power spectrum on cluster abundances can also be seen in models B and C which have the same σ_8.

Thus, a crucial test of a given model such as CDM is whether the theoretical cluster catalogs agree with observed cluster and group catalogs. Of course, many people have pointed to the sensitivity of cluster abundances to the biasing factor in the past. However, although it has been known since the beginnings of the biased CDM model that high biasing factors (low σ_8) yield anemic clusters (e.g., BBKS) and that this could serve as a powerful test of the model, there was no confirmation that either the "single-filter peak" or Press-Schechter method worked on the extreme rare event side; and there was little justification for the mass and velocity formulas adopted. Within the past few years, there have been a number of attempts to calibrate the Press-Schechter formula. For example, Narayan & White (1987), Efstathiou et al. (1988), Efstathiou & Rees (1988), and Bond et al. (1991b) used (rather small) *N*-body studies that could only probe a short way into the high-mass rare-event tail. Brainerd & Villumsen (1992) have used high-resolution calculations of a smaller simulation volume to determine the halo mass function on smaller mass scales. Our use of the 128^3 Couchman data in BM2 has "validated" the Press-Schechter formula far out on the tail, and, even more so, has validated the hierarchical peaks model, both spatially and in mass and velocity number densities, lending confidence to our extrapolations to rarer objects than the limited *N*-body studies find.

If the rare events in our cluster catalogs or those constructed from *N*-body simulations are to be used to compare with cluster data, great care must be taken to properly include evolution effects, a point which has often been ignored in cluster literature. For small σ_8, the massive clusters are so rare that there is a large difference predicted between the cluster population at $z = 0$ and the cluster population at $z = 0.1$.

Consider the leading term in the abundance of very massive clusters at redshift z compared with those at $z = 0$, which is a Gaussian. For peaks of height ν at $z = 0$, the abundance ratio is $n(z)/n(z = 0) \sim \exp[-\nu^2 z(1 + z/2)]$. Even over a 200 h^{-1} Mpc box, a typical size for large *N*-body studies of clusters such as the Couchman simulation used in BM2 for "validation," the abundance variation can be substantial. If the near side of the box is at redshift $z = 0$ then the far side is at $z = 0.07$, 3 σ peaks will decrease in density by a factor of 2 over the box. This is very apparent in our simulations of low σ_8 models. For large σ_8, like $\sigma_8 = 1$, there is not as much evolution evident in the neighborhood of $z = 0$; the dramatic dependence occurs earlier, say around $z = 0.5$, when the far side would be at $z = 0.63$, and the abundance drop would be 2.3.

The common practice of taking a constant redshift output from an N-body simulation to compare with cluster data is therefore not accurate; redshift space corrections should be applied *across* the simulation volume (Bond & Myers 1991). For data using Abell catalogs, σ_8 factors should often be corrected by 10% or more because of this. A nice feature of the hierarchical peaks method is that it is easy to include this variable dynamical evolution over a box.

3. UNCERTAINTIES IN CLUSTER PHYSICS WITHIN PEAK PATCHES

The catalogs would not be of much use if they could not be directly compared with observational data. However, the observables of a given cluster probe in detail the interior density profiles of the galaxy, gas and dark matter distributions, and their random velocities. These can only be determined with accuracy by high-resolution hydrodynamical/N-body simulations, and few with the required accuracy are currently available. Progress can be made by using the gross interior properties that we measure with the peaks method in conjunction with observed information for clusters. Whether a given theoretical model of a cluster can actually reproduce observed profiles is an issue for further study.

Consider the optical velocity dispersion data. Often isothermal distributions are assumed and, of course, this is the distribution we can most easily relate to our peak-patch measurements of the initial state, since the single dispersion would be proportional to the binding energy estimate of velocity, $v_{E,\rm pk}$. However, even for such a well studied cluster as Coma, there are many caveats (Merritt 1987; The & White 1987). Factors complicating the translation from the optical velocity observable to our internal energy estimate of the associated peak-patch include: the orbits may be more radial than isotropic, cooler subclusters may not have fully virialized within the cluster potential, the dark matter distribution may not have settled into equilibrium if there were recent mergers, and, even if it has, nonsphericity of the velocity ellipsoid is expected. N-body groups in CDM-like models have dark matter profiles that seem to fit Hernquist (1990) profiles (Dubinski & Carlberg 1991), which are not isothermal. As well, the galaxy velocities may be systematically low relative to dark matter velocities, i.e., velocity biasing may exist (Carlberg & Couchman 1989).

These corrections could add up to sizable uncertainties, which we bundle into a total factor $C_{v,G} = v_{\rm 3D,G}/v_{E,\rm pk}$, which we can think of as a random variable with a mean and a dispersion. If we write the three-dimensional dispersion for the dark matter as $v_{\rm 3D,dm} = C_{v,\rm dm} v_{E,\rm pk}$ and the velocity biasing relation as $v_{\rm 3D,G} = v_{\rm 3D,dm}/b_v$, then $C_{v,G} = C_{v,\rm dm}/b_v$. There are a number of physical effects which will ensure that at least some velocity biasing will be present (Carlberg & Dubinski 1991), but the level is somewhat controversial, although values much in excess of 20% above unity seem unlikely at the current time. If isolated virial equilibrium were to prevail in the clusters, and the galaxies had unbiased velocity fields, we would estimate $C_{v,G} \approx 0.94$ relative to our peak binding energies. If the kinetic energies are better indicators of $v_{\rm 3D}$, we would get $C_{v,G} \approx 1.11$. More study is needed to assess the uncertainty from all of the effects.

X-ray surveys so far provide the best observational data to compare cluster catalogs with. For example, the compilation of all-sky survey data by Edge et al. (1990) provides a flux-limited nearby cluster sample with X-ray temperature information. However, to compare theoretical cluster catalogs with X-ray flux counts, luminosity, and temperature functions, better hydrodynamical models than currently exist are needed to find the cluster density and temperature profiles and how they evolve, so we must again resort to observations (e.g., Mushotzky 1988).

In particular, we assume an isothermal gas with temperature T_X. If the gas and dark matter were both in virial equilibrium in the same gravitational potential, we would have $T_X = \beta_T^{-1} v_{\rm 3D,dm}^2/(3 Y_T m_N)$, where m_N is the nucleon mass, Y_T is the number of particles per baryon, and the factor $\beta_T = 1$. For fully ionized hydrogen and helium, Y_T is between 1.68 and 1.69 for cluster abundances. Although $\beta_T = 1$ corresponds to an isothermal equilibrium, a well-known estimate based upon the comparison with optical velocity data is $\beta_T \approx 1.2$ (e.g., Mushotzky 1988) and Evrard (1990a)'s low-resolution hydrodynamics calculations gave $\beta_T \approx 1.25$. These high values may be due to overestimation of the velocity dispersion of galaxies in clusters (e.g., Edge & Stewart 1991) in the first case. We bundle both $C_{v,\rm dm}$ and β_T uncertainties into a temperature uncertainty $C_T = C_{v,\rm dm}^2/\beta_T$. For a nonisothermal profile, it would be a function of the effective radius of the region within the cluster that the specific observations we are interested in modeling probe. A typical cluster temperature profile may be low in the center because of a cooling flow but have a relatively isothermal region where much of the X-ray emission occurs, with a fall-off at large radius (e.g., Sarazin 1986; Mushotzky 1993). The factor C_T is perhaps 1.2 if we use the kinetic energies to calibrate and take $\beta_T = 1$. Note that this is also close to what the sample constrained collapse described in BM1 gives. Numerically, the temperature becomes

$$T_X = C_T v_{\rm E,pk}^2/(3 Y_T m_N) = 1.5\, C_T (v_{\rm E,pk}/850\ {\rm km\ s^{-1}})^2\ {\rm keV}\,. \quad (3.1)$$

To calculate fluxes and luminosities, we must also know the density profile of the hot intracluster gas within the virialized peak patch. For this, we adopt the standard assumption made in studies of X-ray clusters, a spherical "β-model" for the (uncooled) cluster gas density:

$$n_B = n_{B_c}/(1 + r^2/r_{\rm core}^2)^{3\beta_\rho/2}, \quad r < R_{\rm E,pk}\,. \quad (3.2)$$

We truncate the distribution at $R_{\rm E,pk}$ the Eulerian radius of the peak, which we relate to the Lagrangian radius $R_{\rm pk}$ by $R_{\rm E,pk} = 0.3 R_{\rm pk}/F_{\rm pk}$. (This basically follows from $R_{\rm E,pk} = R_{\rm pk}/(1 + \bar{\delta})^{1/3}$, where $\bar{\delta}$ is the current volume-averaged overdensity.) The total number of baryons within the peak-patch is $B_{\rm pk} = (4\pi/3)\bar{a}^3 \bar{n}_B R_{\rm pk}^3$, where $\bar{n}_B$ is the average baryon density in the universe. These baryons are redistributed into this profile. Given $B_{\rm pk}$, β_ρ, and $r_{\rm core}$, we can determine the central density, n_{B_c}. We take $\beta_\rho = \frac{2}{3}$ and

$$r_{\rm core} = \min\,(f_X R_{\rm E,pk}, r_{\rm core,max}), \quad \text{with } f_X = 0.1,\quad r_{\rm core,max} = 150\, h^{-1}{\rm kpc}\,, \quad (3.3)$$

using best estimates from Mushotzky (1988, 1993), although not much is known about the variation of $r_{\rm core}$ with mass and

redshift. The crossover between the two $r_{\rm core}$ forms occurs around $7 \times 10^{14}\, h^{-1} M_\odot$.

A further uncertainty arises because, over the scale that X-ray observations probe, there may have been some segregation between the gas and the dark matter, as often occurs in dissipative collapses (e.g., Bond et al. 1984; Babul & Katz 1993). One of the current dilemmas in cluster physics is that the gas profile seems to be rising relative to the dark matter profile, at least in Coma, Perseus, and those few other clusters in which the data is good enough to address the issue. The best estimates also indicate that the gas to dark mass ratio within an Abell radius is ~0.2–0.3, or more (e.g., Sarazin 1986; Hughes 1989). The current observational situation, including *ROSAT* results which support the earlier observations of this, is reviewed by Mushotzky (1993). It is unclear whether segregation can explain this or whether it actually reflects the primordial ratio of baryons to dark matter. If segregation occurs, the degree will certainly depend upon radius. The segregation could even go in the opposite direction if significant entropy generation occurs in the medium before the clusters form, e.g., through gas shocking (Bond et al. 1984) or preheating (Evrard 1990b, Kaiser 1991), and the decrease in the baryon density will be most dramatic for lower mass clusters and groups. Without segregation, the baryon to total mass ratio, $m_N B_{\rm pk}/M_{\rm pk}$, is just $\Omega_B/\Omega_{\rm nr}$, where $\Omega_{\rm nr}$ is the density parameter in clustering matter. For the models considered here, the nr-matter consists of baryons, CDM, and hot dark matter (because it is cool enough to cluster on cluster scales). Of course, some of the baryons will have turned into stars and will be stored in galaxies. The gas to total mass ratio will therefore be less than the baryon-to–total mass ratio and may be substantially so for smaller clusters and groups. To parameterize this uncertainty, we introduce yet another correction factor $C_{\rho,g}$ for the gas that lies within some radius r probed by a given set of observations, $M_{\rm gas}(<r)/M_{\rm tot}(<r) = C_{\rho,g} m_N B_{\rm pk}/M_{\rm pk}$. This parameter may vary from observation to observation. Finally, there is uncertainty in the primordial nucleosynthesis value of Ω_B. For the $h = 0.5$ cases shown here, we have used the preferred value of $\Omega_B = 0.05$ to normalize the result (e.g., Walker et al. 1991). We can bundle all of these uncertainties into an effective baryon density parameter $\Omega_{B\rm eff} = C_{\rho,g}\Omega_B$.

4. SIMULATIONS OF NEARBY ALL-SKY X-RAY CATALOGS

Using these parameterizations of our state of ignorance of interior cluster physics, we can apply our peak-patch catalogs to X-ray observations. We only use bremsstrahlung emission for the results described here, although all processes that participate in cluster cooling should be included, in particular the recombination and line cooling that dominate cooling flows. For bremsstrahlung, the luminosity goes as $L_X \propto T_X^{1/2} C_{\rho,g}^2 B^2/(r_{\rm core} R_{\rm E,pk}^2)$, which leads to an uncertainty factor $C_{L_X} = \Omega_{B\rm eff}^2 C_T^{1/2}/C_{r_{\rm core}}$, where $C_{r_{\rm core}}$ is a core radius correction factor. The uncertainty in the fluxes C_{S_X} has a slightly different form and is sensitive to the details of the observational strategy.

In Bond & Myers (1991, 1993b), we have estimated σ_8 using the hierarchical peaks method applied to the flux-limited Edge et al. sample. The Edge et al. sample gives results compatible with those found with *ROSAT* and *ASCA*. We present those results here, since they illustrate another important use of our Monte Carlo method: we use it to check in detail that the analytic counterpart of the hierarchical peaks theory (developed in BM4) gives reliable results. To model the Edge et al. selection procedure, we use the hierarchical peaks technique to simulate 27 contiguous boxes of size 200 h^{-1} Mpc arranged in a cube that encompasses a sphere of radius 300 h^{-1} Mpc about us, and therefore can be used as a data set for an all sky survey extending to $z = 0.108$. The Edge et al. data went out slightly further, so we also applied this redshift cut to their clusters, which left 44 out of their original 46 clusters that were within such a volume limit.

To give a visual illustration of the large differences that the various models predict for velocity dispersions and temperature data, we use the all-sky catalog constructed from the simulations in Figure 2 to plot Hammer-Aitoff projections of the peak-patches between 20 h^{-1} Mpc and 300 h^{-1} Mpc (i.e., redshift 0.108) with $v_{E,\rm pk} > 1070$ km s^{-1}, corresponding to X-ray

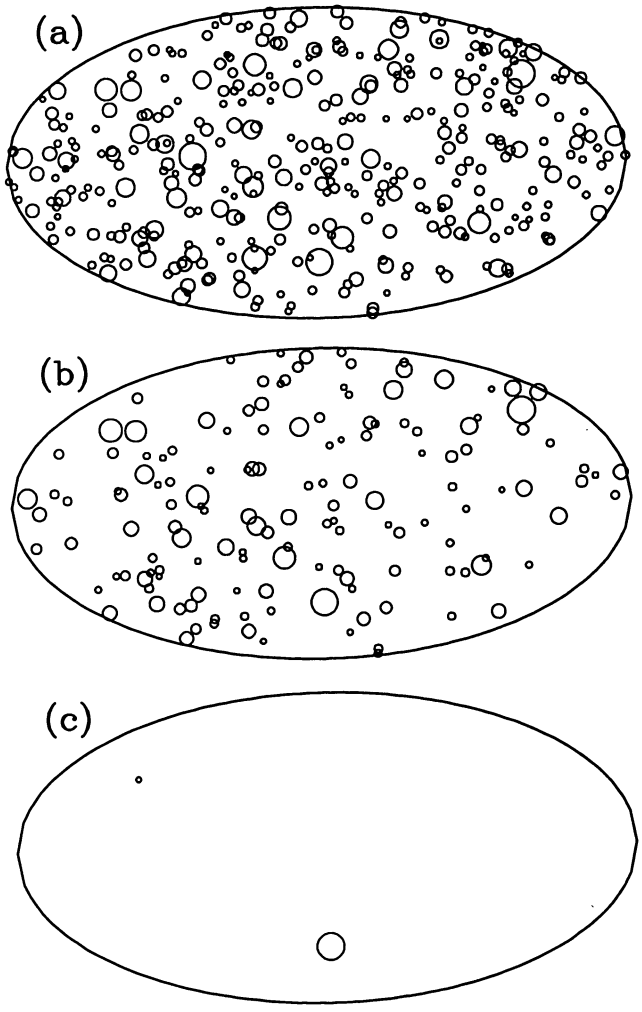

FIG. 2.—Hammer-Aitoff projections of the peak-patches with redshift ≤ 0.1 found in the 27 box simulations, whose velocities $v_{\rm E,pk}$ estimated from internal energy lie above 1070 km s^{-1}, corresponding to X-ray temperatures of $T_X > 2.4\ C_T$ keV. The size of the circles scale with $v_{\rm E,pk}$. (*a*) shows the CDM model A, with $n_s = 1$ and $\sigma_8 = 1$; (*b*) shows a CDM model with $n_s = 1$, but $\sigma_8 = 0.71$; (*c*) shows the $\Gamma = 0.2$ CDM model, with $n_s = 1$ and $\sigma_8 = 0.45$. The maximum circle size saturates at 2500 km s^{-1}.

temperatures $T_X > C_T 2.4$ keV. The size of the circles scales with velocity dispersion, saturating at 13 keV. We plot models A and C in the top and bottom panels. With such a high cut, the differences between models B and C are not that great. Instead, for the middle one, we show a $\sigma_8 = 0.71$ CDM model with $n_s = 1$. There are 349, 144, and 2 clusters in the panels, respectively. There would be a few more smaller velocity dispersion clusters in Figure 2*c* if we used a $\Gamma = 0.5$ power spectrum, like standard CDM, rather than a $\Gamma = 0.2$ one.

To be more quantitative in comparing with the data, we plot various X-ray one-point functions in Figure 3. We show the results of the 27 box simulations for the $\sigma_8 = 1$ CDM model (A) and the $\sigma_8 = 0.45$ $\Gamma = 0.2$ model (D) for the temperature and luminosity functions by open circles. Note that the Monte Carlo data for model D falls slightly below the analytic result. This is because there are so few clusters in the 27 boxes. Although the analytic method uses mean-field properties of peak-patches, whereas we have seen in BM2 that there is considerable scatter in the individual properties of clusters, the semi-analytic theory does *extremely* well. The semi-analytic results

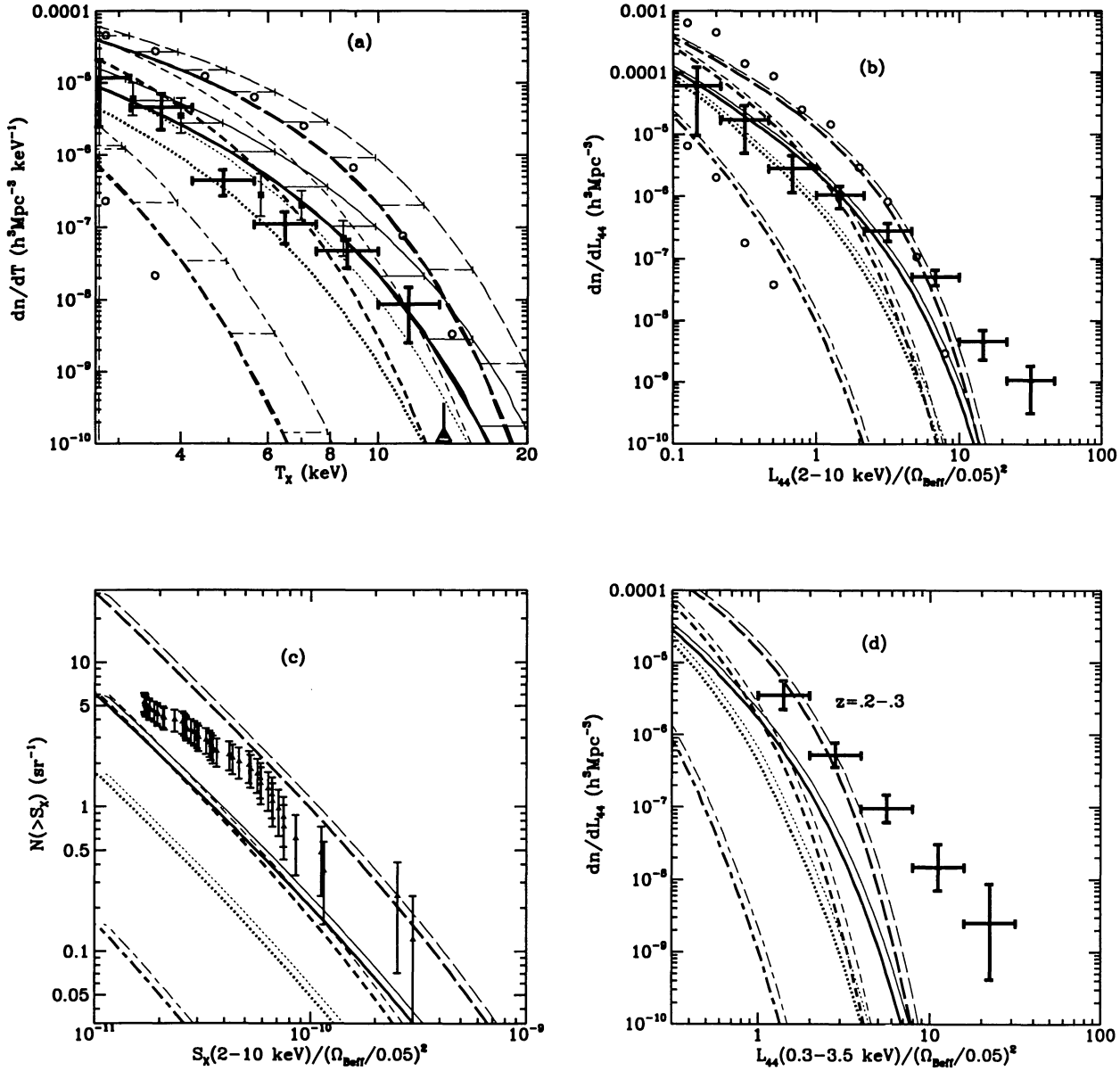

FIG. 3.—Comparison of the peak-patch predictions for wedge models A–D with the Edge et al. (1990) X-ray data is shown for the temperature function (*a*), the 2–10 keV luminosity function (*b*) and flux counts per steradian (*c*). Model A is large-dashed; model B, short-dashed; model C, solid; and model D, long-short-dashed. The dotted curve is model C, but with $\sigma_8 = 0.6$ rather than 0.71. Heavier curves have $C_T = 1.0$ and lighter ones have $C_T = 1.23$, and the joining "error bars" indicate the plausible range. The numerical results from the 27 box Monte Carlo simulations (*circles*) for models A and D show the analytic calculations are accurate. (*a*) The Henry and Arnaud dn/dT (*squares*) and an abundance corresponding to one 13.6 keV cluster within $z = 0.2$ (*triangle*). (*d*) The EMSS $z = 0.2$–0.3 luminosity function in the energy band 0.3–3.5 keV. The $(\Omega_{Beff}/0.05)^2$ uncertainty in (*b*), (*c*), and (*d*) could make low σ_8 models more compatible with the data.

for models B and C are also shown in this graph. We also include model C with $\sigma_8 = 0.6$ to show the sensitivity to small changes in σ_8 and to bracket the temperature data. The error bars, when present, are assigned assuming Poisson statistics for the cumulative and binned differential counts. The 2–10 keV flux limit of 1.7×10^{-11} ergs cm^{-2} s^{-1} used by Edge et al. was used to construct this figure. The luminosities were derived assuming $h = 0.5$ as for the models considered here. The luminosities scale with $(2h)^{-2}$. To demonstrate the predictive power of the method for evolutionary aspects of the X-ray luminosity function, we compare in Figure 3*d* our theoretical models with the *Einstein* Medium Sensitivity Survey (EMSS) data of Gioia et al. (1990) and Henry et al. (1992) for intermediate-redshift clusters.

Just as the wedge diagrams indicate, Figure 3 shows that high-bias models, such as D, fail to produce significant numbers of high-temperature and luminosity clusters, in marked contrast to the available data. On the other hand, the $\sigma_8 = 1$ model overproduces high-temperature clusters. The best-fit value of σ_8 depends upon the temperature correction factor; it is $\sim$0.7 for $C_T = 1$ and about 0.6 for $C_T = (1.11)^2$ (as suggested by $v_K/v_{E,\mathrm{pk}}$). Thus we would estimate $\sigma_8 \sim 0.6$–0.7 from the temperatures alone, whereas values of σ_8 between 0.7 and 1 are suggested by the luminosity and flux data, (Figs. 3*b* and 3*c*), but, because of the strong $(\Omega_{B\mathrm{eff}}/0.05)^2$ scaling uncertainty, smaller values of σ_8 are certainly feasible. The models with enhanced large-scale power and less small-scale power than standard CDM fit the shape of the Edge et al. curves better. Kaiser (1991), Evrard & Henry (1991) and Henry & Arnaud (1991) also argued that flatter power-law spectra agree better with the Edge et al. data. On the other hand, perhaps variations in internal physics as one goes from low- to high-mass clusters could explain it.

If we can accept the EMSS results at face value, none of the models can reproduce the relatively large space density of bright clusters seen at redshifts $z = 0.2$–0.3. And all of the models fall short of reproducing the flat EMSS luminosity function, although the $(\Omega_{B\mathrm{eff}}/0.05)^2$ scaling uncertainty (possibly mass-dependent) can help to get compatibility. A highly flattened $\sigma_8 = 1$, $\Gamma = 0.1$ model, which does *not* match the *COBE* or low-redshift X-ray data, can reproduce the EMSS shape (Bond & Myers 1991, 1993b), but it and other high σ_8 models do not show the significant steepening with increasing redshift that Gioia et al. (1990) and Henry et al. (1992) report. Models with nonzero cosmological constant are rather successful in matching the data.

In our original estimations of σ_8 from the X-ray data (Bond & Myers 1991), we took $C_T = 1$, $C_{L_X} = 1$, and $C_{S_X} = 1$ and concluded that the results were bracketed by two CDM models with $\sigma_8 = 0.65$ and $\sigma_8 = 0.93$. The uncertainties which allow lower values were better addressed in Bond & Myers (1993b), and more cases were calculated, a subset of which is shown in Figure 3. Our σ_8 result was in strong disagreement with Frenk et al. (1990), who estimated 0.4–0.5 from optical velocity data and the Edge et al. temperature distribution. The Frenk et al. paper pioneered the use of Monte Carlo cluster samples, albeit built from relatively small N-body simulations, and showed that projection effects could strongly bias the optically determined velocities to high values. We believe that their corrections were too strong. Using different methods than in the Frenk et al. paper, White et al. (1993) increased their estimate to $\sigma_8 = 0.55 \pm 0.05$. Part of the discrepancy with our estimate of σ_8 may be due to the region of the spectrum being probed. That is, if the actual spectrum is flatter than the CDM one, those who probe farther out in mass would normalize CDM with a higher σ_8 than those who probe smaller scales; and the Edge et al. (1990) data do prefer a flattened spectrum relative to CDM. The Frenk et al. (1990) calculations had only 64^3 particles covering a $(180\ h^{-1}\ \mathrm{Mpc})^3$ volume. We note that Evrard (1990a) focused on the large mass range and got $\sigma_8 \approx 0.6$. A 10% correction or so should be applied to all of their estimates because the average cluster redshift is not zero, which they assumed. If we use our $C_T = 1.23$ number and this correction, their σ_8 estimates become compatible with ours.

Henry & Arnaud (1991) considered constraints on power-law fluctuation spectra from an X-ray temperature distribution function they derived for a flux-limited sample of 25 clusters within $z = 0.9$. They used the Press-Schechter formula and the calibration of the $T_X - M$ relation from Evrard's (1990a) 16^3 hydro simulations of clusters. They obtained $\sigma_8 = 0.59 \pm 0.02$ and a (local) spectral index $n_s = -1.7^{+0.65}_{-0.35}$ which is substantially flatter than the $n_s \approx -1$ that the CDM model gives in the cluster region. We have included the Henry & Arnaud abundances as squares on Figure 3*a* to be a foil to the Edge et al. data. Bartlett & Silk (1992) have compared *COBE*-normalized models to the Edge et al. temperature data as well, also using the PS formula with Evrard's $T_X - M$ relation. For the model C case which we can directly compare with their result, the Bartlett & Silk (1993) estimate of dn/dT is a little higher than ours. Henry & Arnaud (1991) and Bartlett & Silk also did not include evolutionary corrections which would bring their numbers into closer agreement with ours, especially if we use the kinetic energy calibration for C_T.

Arnaud et al. (1992) used data from the *Ginga* satellite to identify A2163, a cluster at redshift ~ 0.2 with the very high X-ray temperature $T_X = 13.6$ keV. Obviously, this strongly constrains how low σ_8 can be provided the cluster emission is not confused by other sources in the *Ginga* "beam" and complex gas physics does not modify the fully virialized assumption. Adams et al. (1993) used the analytic version of the hierarchical peak-patch theory to show that $\sigma_8 \gtrsim 0.7$ is needed to get at least one $T_X = 14$ keV cluster at redshift 0.2 for tilted CDM models such as A and B. Although the curves in Figure 3*a* correspond to the Edge flux-limited catalog, with a redshift 0.1 cutoff, we denoted a lower limit on the cluster abundance appropriate for *one* 13.6 keV cluster within a spherical volume of radius $573\ h^{-1}$ Mpc (i.e., redshift 0.2 for Einstein–de Sitter models) by a large triangle. The stronger evolutionary effects would make the curves fall off even faster for a given model. We see from Figure 3*a* that we do not have to go much beyond $\sigma_8 \sim 0.7$ to be able to explain the *Ginga* observation; indeed, with $C_T = 1.23$, even the $\sigma_8 = 0.6$ model with the flattened hot/cold hybrid spectrum can give such a 14 keV cluster, although it would be more likely to be at $z \sim 0$ than at $z \sim 0.2$. Tens of such clusters would be predicted with $\sigma_8 \sim 1$, and they do not seem to be out there in such numbers. Indeed, we note that the richest cluster in Abell's catalog, A665 at $z = 0.18$, has a more modest $T_X = 8.2$ keV, so it is unclear how (un)representative A2163 will turn out to be. In fact, the A665 Sunyaev-Zeldovich decrement is now well observed, giving a $\Delta T/T = -1.46 \times$

10^{-4} between cluster center and cluster outskirts (Birkinshaw, Hughes, & Arnaud 1991), which also agrees reasonably well with estimates obtained from the X-ray observations of bremsstrahlung from the hot cluster gas. Carlberg et al. (1993) presented preliminary optical velocity dispersion data for a subsample derived from the EMSS, which also indicates a high normalization, in the range $0.7 \lesssim \sigma_8 \lesssim 1.0$. Couchman & Carlberg (1992) raised the spectre of σ_8 being in excess of unity, with the explanation of the paucity of very high velocity dispersion clusters a result of velocity biasing in which $v_{3D,G}/v_{3D,dm}$ is substantially below unity; however, a large temperature biasing of X-ray clusters would also be required, and this does not seem likely.

Although we think a value of σ_8 around 0.7 for $\Omega_{nr} = 1$ models gives a cluster distribution that offers the best hope for explaining current data—as did Bond (1988) and Cole & Kaiser (1988), but for less precise reasons—it is certainly premature to suppose that σ_8 has been accurately pinned down. The internal cluster physics needs to be better understood and the data needs to be much improved before we can regard the estimates as reliable. Impressive new cluster samples offered by *ROSAT*, *ASCA*, and various cluster redshift surveys, along with the burst of theoretical work stimulated by the new data, will warrant a more detailed confrontation with these new data bases in the near future.

5. X-RAY AND SZ MAPS FROM DEEP PEAK-PATCH CATALOGUES

The ultrahot ionized gas in the intracluster medium produces both the thermal bremsstrahlung X-ray emission discussed above as well as Compton scattering of the microwave background radiation—this latter process is known as the Sunyaev-Zeldovich (SZ) effect. Although for many years measurements of the SZ effect were plagued by difficulties, it is now the case that measurement and, in an increasing number of cases, imaging of the SZ effect in clusters is a reliable, if not routine, endeavor. Solid observations now exist for around a dozen clusters ranging in redshift from $z = 0.023$ (Coma: Herbig, Lawrence, & Readhead 1995) to $z = 0.545$ (0016+16: e.g., Birkinshaw 1990).

The SZ effect has great utility for the study of the state of the cluster gas, which in turn can be used to constrain cosmological models and determine parameters such as H_0 and q_0. Because the Compton scattering depends upon the electron pressure $n_e T_e$, while the bremsstrahlung emission follows $n_e^2 T_e^{1/2}$, the integral equations for the two effects can be solved assuming a radial density profile $n_e = n_0 f(r; r_c)$ which is parameterized by a scale length or "core radius" r_c (e.g., the beta model of eq. [3.2]). By comparison with the observed X-ray or SZ profile on-sky, the apparent core radius θ_c can be used to determine the angular diameter distance and thus H_0 and q_0 given a suitable sample of target clusters.

In addition, because the SZ effect is proportional to the electron density, it probes the intracluster medium out to much larger radial distance than the X-ray emission. This, in turn, will provide tight limits upon the total baryonic mass in the cluster, without the usual bias toward the high-density central regions.

Given the assumptions about the internal physics of clusters, we can transform the $5° \times 5°$ wedge catalogs into $5° \times 5°$ X-ray and Sunyaev-Zeldovich maps of the sky, which can then be used as a testbed upon which to evaluate the effectiveness of various experiments for probing cosmological models. In turn, the simulated images derived from our peak-patch catalogs can be used to optimize the design of new experiments.

5.1. *Simulated Images of Cluster X-Ray Emission and the SZ Effect*

For the X-ray maps, we choose the *ROSAT* PSPC parameters in pointing mode. We passed the redshifted bremsstrahlung spectrum for each cluster through an approximate *ROSAT* filter (0.1–2.4 keV) to get the sky surface brightness of these sources. The *ROSAT* maps are shown in Figure 4. We have not applied any filter to the maps, since the pixel size in the map is 35″, about the *ROSAT* resolution in pointing mode. However, beyond the inner 40′ of the total 2° *ROSAT* field of view, the resolution is degraded. The minimum contour level of $2.5 \times 10^{-15}\, C_T^{1/2} (\Omega_{B\mathrm{eff}}/0.05)^2$ ergs cm^{-2} s^{-1} is indicative of what a long-exposure pointed *ROSAT* observation can achieve (e.g., White et al. 1993). Subsequent contours increase by a factor of 2 over previous ones. These maps graphically illustrate that the deep *ROSAT* observations look promising for differentiating, at the very least, the $\sigma_8 = 1$ model from the $\sigma_8 = 0.45$ one, subject of course to the caveat that there is a substantial $\Omega_{B\mathrm{eff}}^2$ uncertainty. Note that some of the clusters near the boundary apparent in some of the maps are outside the boundary in other maps due to different Zeldovich dynamics. The *ROSAT* all-sky survey 5 σ sensitivity is somewhat worse than the prelaunch estimate of $\sim 2 \times 10^{-13}$ ergs cm^{-2} s^{-1}. Maps constructed with the all-sky survey parameters and this sensitivity are not very rich in clusters; a useful map would cover a region much bigger than $5° \times 5°$.

The "Sunyaev-Zeldovich" anisotropy from upscattering of the microwave background photons by the hot intracluster gas in a given direction is proportional to the line-of-sight integral of the electron pressure $n_e T_e$ (e.g., Sunyaev & Zeldovich 1980). The $5° \times 5°$ maps corresponding to the X-ray maps are shown in Figure 5. The microwave background decrements in the SZ maps were calculated for an observing frequency of 20 GHz and a Gaussian beam of 1.′8, which corresponds to the parameters of the Readhead et al. (1989) and Myers, Readhead, & Lawrence (1993) OVRO experiments. The contours are negative, dropping by factors of 2 from the starting value of $-2.5 \times 10^{-6} (\Omega_{B\mathrm{eff}}/0.05) C_T$. The central decrement scales as $(\Omega_{B\mathrm{eff}}/0.05) C_T / C_{r_{\mathrm{core}}}^2$, which is a relatively dramatic dependence upon the core radius, but is not as sensitive to the baryon density uncertainties as the X-ray flux data is. The SZ map mean values (in units of this scaling) are (*a*) -3.2×10^{-6}, (*b*) -0.87×10^{-6}, (*c*) -0.46×10^{-6}, and (*d*) -0.05×10^{-6}. Extrapolated to zero frequency, the SZ decrement is $\Delta T/T = -2y$, so the average Compton y-parameter is half of this Rayleigh-Jeans value (and of opposite sign). Of course, these average y-values are so small because there is little effect along most lines of sight. The minima in the SZ maps are determined by the largest excursions in y. With the 1.′8 beam smearing, the $(\Delta T/T)_{\mathrm{min}}$ are (*a*) -228×10^{-6} (*b*) -107×10^{-6}, (*c*) $-108 \times$

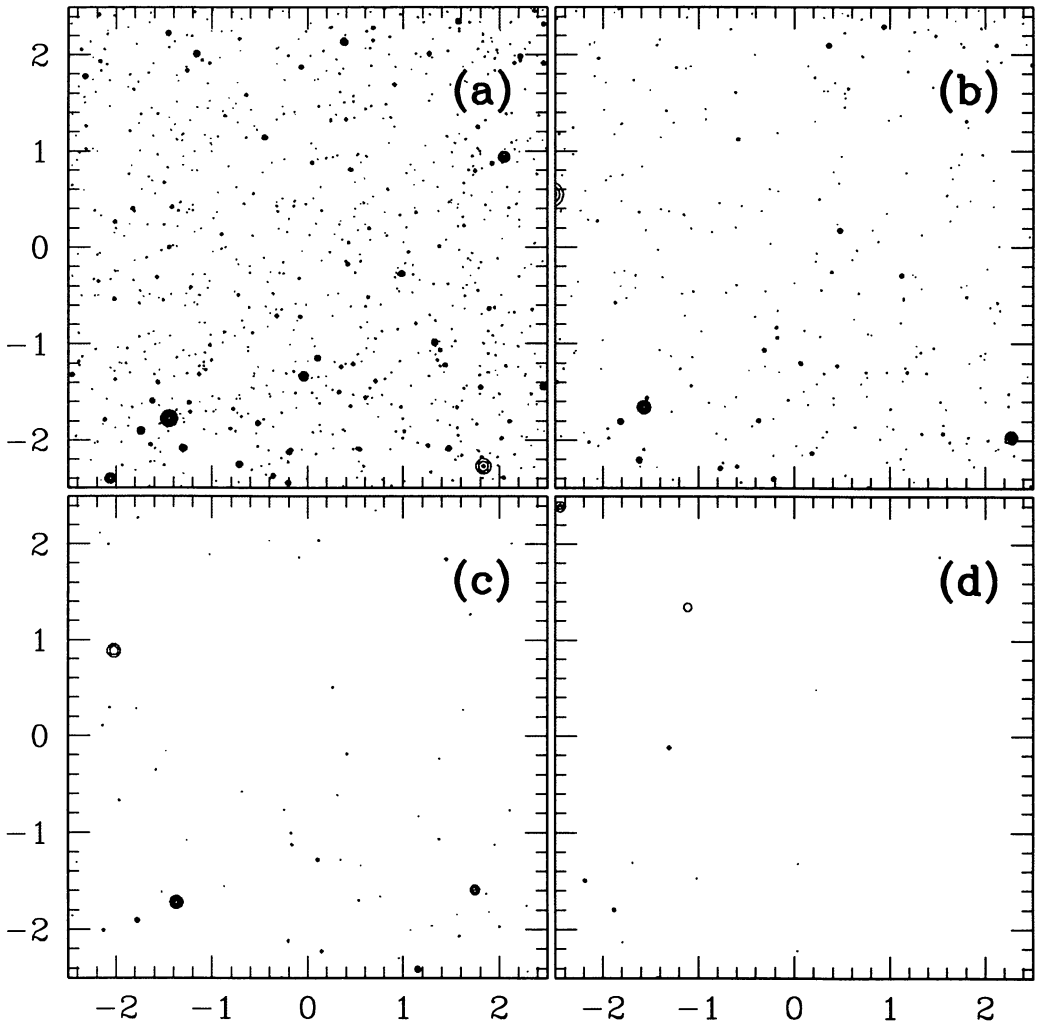

FIG. 4.—(*a–d*) X-ray (*ROSAT*) maps for the "wedge" diagram models A–D. The redshifted bremsstrahlung spectrum for each cluster was passed through an approximate *ROSAT* filter (0.1–2.4 keV) to get the sky surface brightness of these sources. The minimum contour is at $10^{-14}\,(\Omega_{B\mathrm{eff}}/0.1)^2\,C_T^{1/2}$ ergs cm^{-2}s^{-1}, a level similar to the *ROSAT* 5 σ sensitivity for long-exposure pointed observations, and subsequent contours increase by a factor of 2 over previous ones. The gas was assumed to be isothermal with a core radius of $r_{\mathrm{core}} = \min(0.1\,R_{\mathrm{E,pk}}, 150\,h^{-1}\mathrm{kpc})$. C_T is a temperature correction factor, and $\Omega_{B\mathrm{eff}}$ is the effective baryon abundance.

10^{-6}, (*d*) -7.5×10^{-6}. With no beam smearing, the minima are ~15% higher. Although the non-Gaussian aspects of the maps are obviously fundamental for designing experimental strategies to search for the ambient SZ effect, since the anisotropy power is concentrated in cold spots, the rms anisotropy levels, $(\Delta T/T)_{\mathrm{rms}}$, do indicate basic power differences among the maps. These are (*a*) 6.6×10^{-6}, (*b*) 2.8×10^{-6}, (*c*) 2.6×10^{-6}, (*d*) 0.28×10^{-6}.

Because the spectral dependence of the SZ effect is a function of the redshift invariant $h\nu/kT$, the SZ effect is essentially redshift independent, i.e., a cluster with a given set of physical parameters will produce the same central Compton y no matter the redshift at which it is placed. Thus, the SZ effect offers us the opportunity to discover and study those very distant clusters that have formed at early times. These objects would be prohibitively faint in the X-ray wavebands. In fact, a good indicator of distance to the clusters shown in Figures 4 and 5 is the relative strength of the X-ray emission compared to the SZ decrement. Only the nearest most massive clusters appear in the *ROSAT* images.

In addition to the "thermal" Compton scattering, there is also a bulk velocity induced Doppler component to the SZ effect, which manifests itself most strongly near the SZ null at 200 GHz. It has long been noted that measurements of this effect can yield a direct measurement of the peculiar velocity of clusters along the line of sight; with current bolometer array technology, it is in fact now possible to observe this phenomenon (e.g., Wilbanks et al. 1994). As an illustration of the magnitude of the SZ velocity effect, we have generated maps corresponding to those from Figure 5, constructed from the four hierarchical peaks catalogs shown in the "wedge" diagrams. These are shown in Figure 6. Note that nonlinear corrections have *not* been applied to the velocities, hence there is a velocity correction factor $C_V \sim 1.2$.

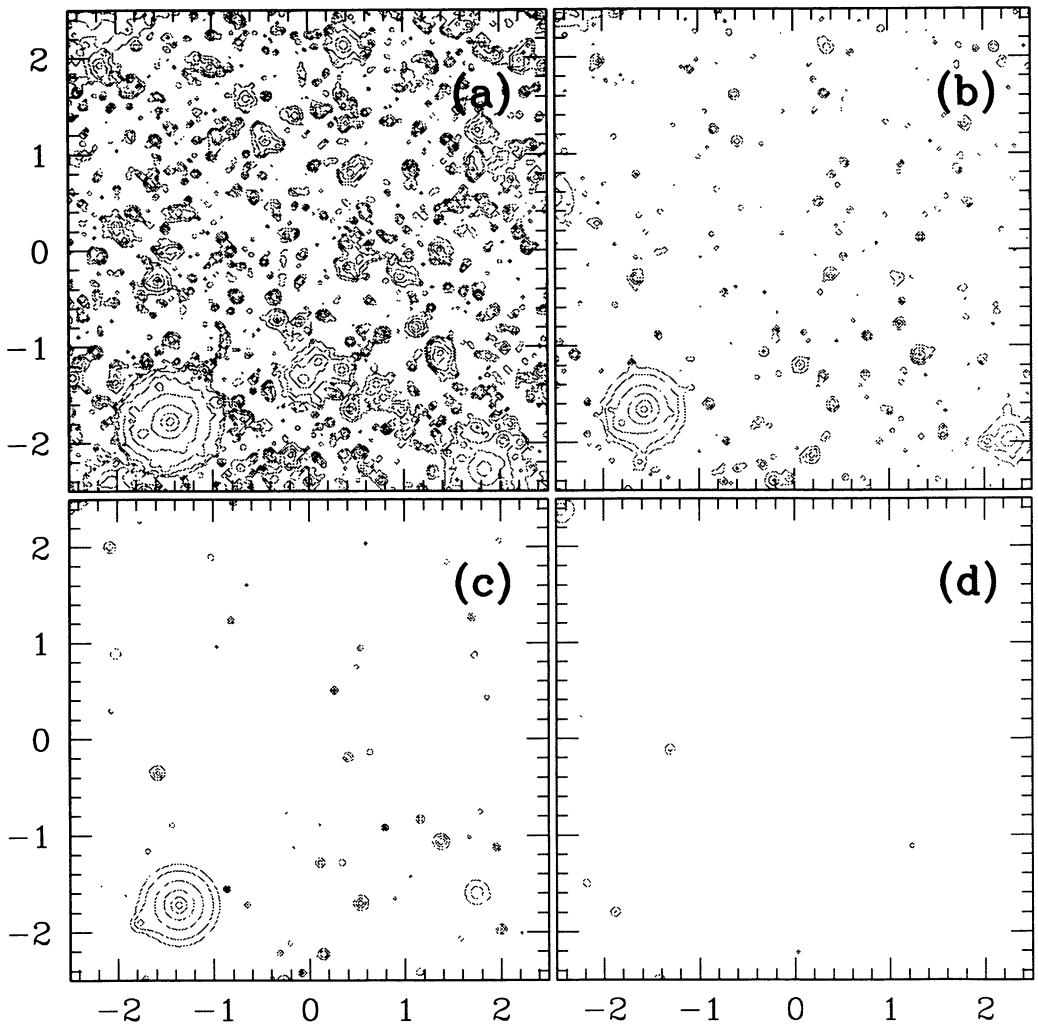

FIG. 5.—(*a–d*) Sunyaev-Zeldovich maps corresponding to the *ROSAT* maps, for 5° × 5° simulated patches of the sky, constructed from the four hierarchical peaks catalogues shown in the "wedge" diagrams, A–D. The contours shown are negative, dropping by factors of 2 from the starting value of $-5 \times 10^{-6}(\Omega_{B\text{eff}}/0.1)C_T$, where C_T is a temperature correction factor, and $\Omega_{B\text{eff}}$ is the effective baryon abundance. The SZ maps are for observations at 20 GHz smoothed with a 1.'8 FWHM Gaussian beam, the parameters of the OVRO experiment.

5.2. *Statistics of the "Ambient" SZ Effect*

We find that primary anisotropies of the background radiation exceed the ambient SZ effect for models A–D. Primary anisotropies are those associated with linear processes occurring at $z \approx 1000$, especially Thomson scattering from moving electrons, photon compression, and gravitational redshifts induced by the perturbed metric (e.g., Bond 1988). In Figure 7, we compare the angular power spectra, C_l, derived from the maps with the power spectra for the primary anisotropies of the CDM model A. The power spectrum C_l is defined as the variance in the multipole coefficient a_{lm} of the microwave background anisotropy pattern $\Delta T(\hat{q})/T$, where $-\hat{q}$ is the angular direction of the incoming photons:

$$C_l \equiv \langle |a_{lm}|^2 \rangle, \quad \text{where } \frac{\Delta T}{T}(\hat{q}) = \sum_{lm} a_{lm} Y_{lm}(\hat{q}) . \quad (5.1)$$

The $Y_{lm}(\hat{q})$ are the usual spherical harmonics. For primary anisotropies and Gaussian initial perturbations, only C_l is needed to fully specify a realization of the anisotropy pattern. For SZ and other secondary anisotropies which are generically non-Gaussian, an infinite number of higher order (reduced) correlation functions of a_{lm} is needed to realize the patterns.

Since the SZ maps are limited to 5° × 5°, one cannot get an adequate power spectrum beyond the fundamental mode of the map, $2\pi/5°$. Expressing this in inverse radians gives the associated minimum multipole $l \approx 72$. Because this is so high, it is adequate to Fourier transform the map to estimate its power spectrum, with l given by the modulus of the angular wavevector $\boldsymbol{l}$. The Nyquist multipole for the 512^2 map is 18,438. The Gaussian filter scale associated with the OVRO beam size of 1.'8 is 4494. (We can roughly consider l to be in inverse radians, so the l-pole probes angles around $3438/l$ arcminutes.)

In Figure 7, we actually plot $l(l+1)C_l/(2\pi)$, basically the power per log of wavenumber. The $l(l+1)$ is included to make the spectrum of the primary anisotropies flat for a scale invari-

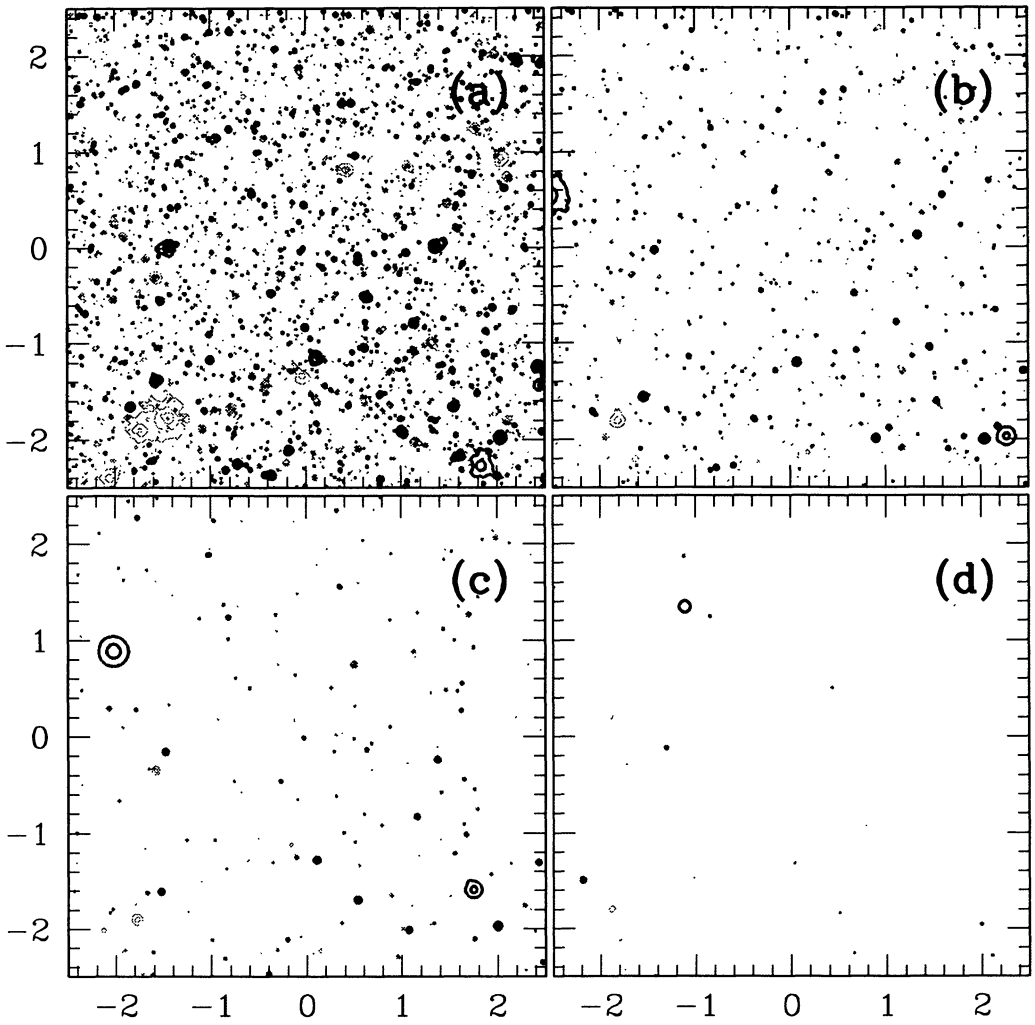

FIG. 6.—(*a–d*) Anisotropy maps from nonlinear Thomson scattering off the hot gas in the cluster streaming with the cluster bulk flow, for 5° × 5° simulated patches of the sky, constructed from the four hierarchical peaks catalogues shown in the "wedge" diagrams, A to D. The heavier contours are positive, the lighter negative. The contour levels increase by factors of 2 from the starting value of $\pm 1.25 \times 10^{-6}(\Omega_{B\text{eff}}/0.1)C_V$, where C_V is a bulk velocity correction factor (~ 1.2), and $\Omega_{B\text{eff}}$ is the effective baryon abundance. No nonlinear corrections were applied to the velocities, hence $C_V \sim 1.2$. The maps are not smoothed, but a 1.′8 FWHM smoothing does not make a large difference.

ant fluctuation spectrum, as is the case at small l for the standard CDM model shown. The primary anisotropy spectrum, taken from Bond et al. (1994), lies above the SZ spectrum down to a few arcminutes. If the CDM model undergoes early reionization, then there is little primary power on scales $l >$ 100, and SZ fluctuations would be the dominant source of fluctuations between $\sim 1°$ and a few arcminutes. For standard recombination, one would have to rely on the spectral differences and the non-Gaussian source-like character of the SZ anisotropies to disentangle the two signals. If one constructs larger SZ maps, one gets a little more power for smaller l.

We also show in the lower panel the multipole band that a few selected microwave anisotropy experiments are sensitive to, utilizing a filter W_l (Bond 1989b) such that the rms fluctuations in a given experimental field would be

$$(\Delta T/T)^2_{\text{rms}} = \sum_l (2l+1)W_l C_l/(4\pi) . \qquad (5.2)$$

These experiments were not designed to look for the ambient SZ effect. The MAX experiment of Meinhold et al. (1993) and Gunderson et al. (1993) is typical of those with a FWHM beam size of 30′. It has a multipole range ideal for optimizing the signal from power spectra like that for the primary anisotropies. A filter with a beam like that of SP91 (Gaier et al. 1992) is better for probing primary anisotropies if early reionization occurred. OVRO filters are good for the SZ effect, especially the new OVRO22 experiment with a 7.′4 beam and a 22.′16 throw. Herbig et al. (1994) and Myers et al. (1995) used this observing strategy to detect the SZ effect in nearby clusters. Note that the *COBE* DMR experiment (Smoot et al. 1992) probes $l \lesssim 20$, and is therefore not of much interest for SZ anisotropies.

Very small angle experiments such as those using submillimeter telescopes (JCMT) are not effective unless one is looking at specific clusters. The VLA is a poor match to the extended SZ effect since the elements cannot be moved close enough

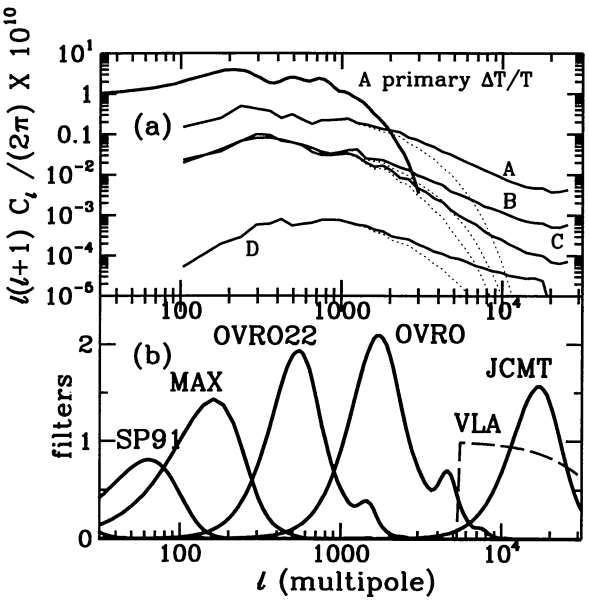

FIG. 7.—(*a*) Angular power spectra for the SZ effect from groups and clusters are contrasted with that for primary anisotropies with standard recombination (model A, with $\Omega_B = 0.05$). The light dotted curves are derived from the 5° × 5° maps with a FWHM of 1.′8, and the heavier solid curves from maps with no beam-smearing. Larger scale maps give more power at low l than shown here. (*b*) Experimental filters W_l as a function of the multipole l. When multiplied by the spectra shown in (*a*) and integrated over ln l, they give the variance in anisotropy expected in each field of the relevant experiment. The DMR filter cuts off at $l \gtrsim 19$. The MAX filter (30′ beam) is for a balloon-borne experiment using bolometers, and the SP91 filter used HEMT receivers at the south pole (90′ beam). OVRO, with a 1.′8 beam, and OVRO22, with a 7.′4 beam, have both been used for SZ detections. "VLA" roughly corresponds to the VLA in *D*-mode at 8.5 GHz and "JCMT" denotes a typical filter for experiments using submillimeter telescopes.

together to prevent excessive loss of temperature sensitivity. Other interferometers provide a better match—the Ryle telescope has been used successfully to measure the SZ effect at 15 GHz in several intermediate-redshift clusters (Jones et al. 1993; Grainge et al. 1993), as has the OVRO millimeter-wave interferometer at 32 GHz (Carlstrom et al. 1995)—because the telescopes can be placed in a close-packed configuration. In addition, the 18- and 10.5-m diameter antennas of these respective arrays provide a field of view of ~4′.

We now describe how the non-Gaussian nature of the distribution of microwave decrements manifests itself for realistic experiments. The map shown in Figure 5 has a decrement distribution which is negative and clearly skewed with a few rare clusters providing very large excursions. In a realistic experiment, chopping on and off source is necessary for atmospheric rejection and gain stability. To get rid of systematic gradients, microwave background experimentalists often use a double differencing scheme, in which the value of the temperature at two points a throw angle $\pm\theta_{\rm throw}$ away from some central point each contribute with weight $-\frac{1}{2}$ to the temperature difference, while the central point contributes +1. Filters for two such chopping strategies are labeled OVRO and OVRO22 in Figure 7*b*. The histograms shown in Figure 8 for these two experiments depict the number of pixels for which a 3 beam chop strategy would yield a value of $\Delta T/T = 10^{-6}D$. Clearly these can be positive as well as negative for a three-beam observing strategy. The histograms are contrasted with two Gaussian curves having noise levels of 27 and 14 μK. Noise levels per point that are this low have already been achieved in microwave background experiments (e.g., Gaier et al. 1992).

Although most random points in the medium have an SZ signal below this noise, there is a significant non-Gaussian tail that can be probed. It appears from Figure 7*b* that OVRO22 with a 7.′4 beam and a 22.′16 throw, using the 5.5 m dish at Owens Valley, is more promising as an instrument to probe the ambient SZ effect than the Owens Valley 40 m dish experiments, with their 1.′8 beam and 7.′15 throw. The $\Gamma = 0.2$ model with $\sigma_8 = 0.45$ has only very tiny deflections D, so it was not worth plotting on the figures. To avoid clutter we only show results for model A, the standard CDM model, and only one of the models with $\sigma_8 = 0.71$; for that we chose model C, the HCDM model with a 7 eV neutrino.

What are the chances that SZ cluster sources will appear in the fields probed by various experiments at a level which can be detected or will affect estimations of the amplitude of primary anisotropies? Our maps can be used to address this question. Consider the Readhead et al. eight-field OVRO experiment and the Myers et al. (1993) 96 field RING experiment. We find that the chance of encountering a SZ source at the 30 μK level in a single field is only 1.3% for CDM model A and 0.14% for HCDM model C. By contrast, in Bond & Myers (1991) we showed that there was a high probability that at least one field would have been contaminated by faint radio sources at the 3 σ level or worse. (One was indeed found.) For the larger beam OVRO22 experiment, the probability of encountering a 30 μK source is higher than for the 1.′8 experiment, 1.5% for model A and 0.6% for model C. Thus, if one makes a small angle map covering hundreds of pixels, then only a few of the fields should be expected to be contaminated with SZ sources.

A comparison of the pixel distributions for CDM primary anisotropy, SZ thermal effect decrements, and SZ velocity effect is shown in Figure 9. Histograms are shown for three three-beam experiments: OVRO7, OVRO22, and the medium-angle MSAM with 28′ FWHM, 40′ throw (Cheng et al. 1994). Also shown is the one-beam distribution for a 7.′5 FWHM beam to illustrate what might be expected from a mapping experiment at these angular scales. Note that in all cases the primary CMB anisotropies dominate over the ambient SZ effects, and it is only the non-Gaussian aspect of the SZ anisotropies that distinguishes them from the CMB.

5.3. *Implications for the Design of SZ Experiments*

We can use the deep peak-patch catalogs to generate simulated maps to compare with the capabilities of proposed instrumentation. In the post-*COBE* era, there are many proposals for the construction of ground-based, balloon-borne, rocket-launched, and space-faring instruments to image the microwave background on angular scales from arcminutes to degrees. Some of these experiments, those aimed at the smaller angular scales, will also be designed to map out the SZ effect in nearby clusters, which have core radii in the range 1′–10′. There is of course the opportunity to discover new clusters through the SZ signature. These would likely be more distant

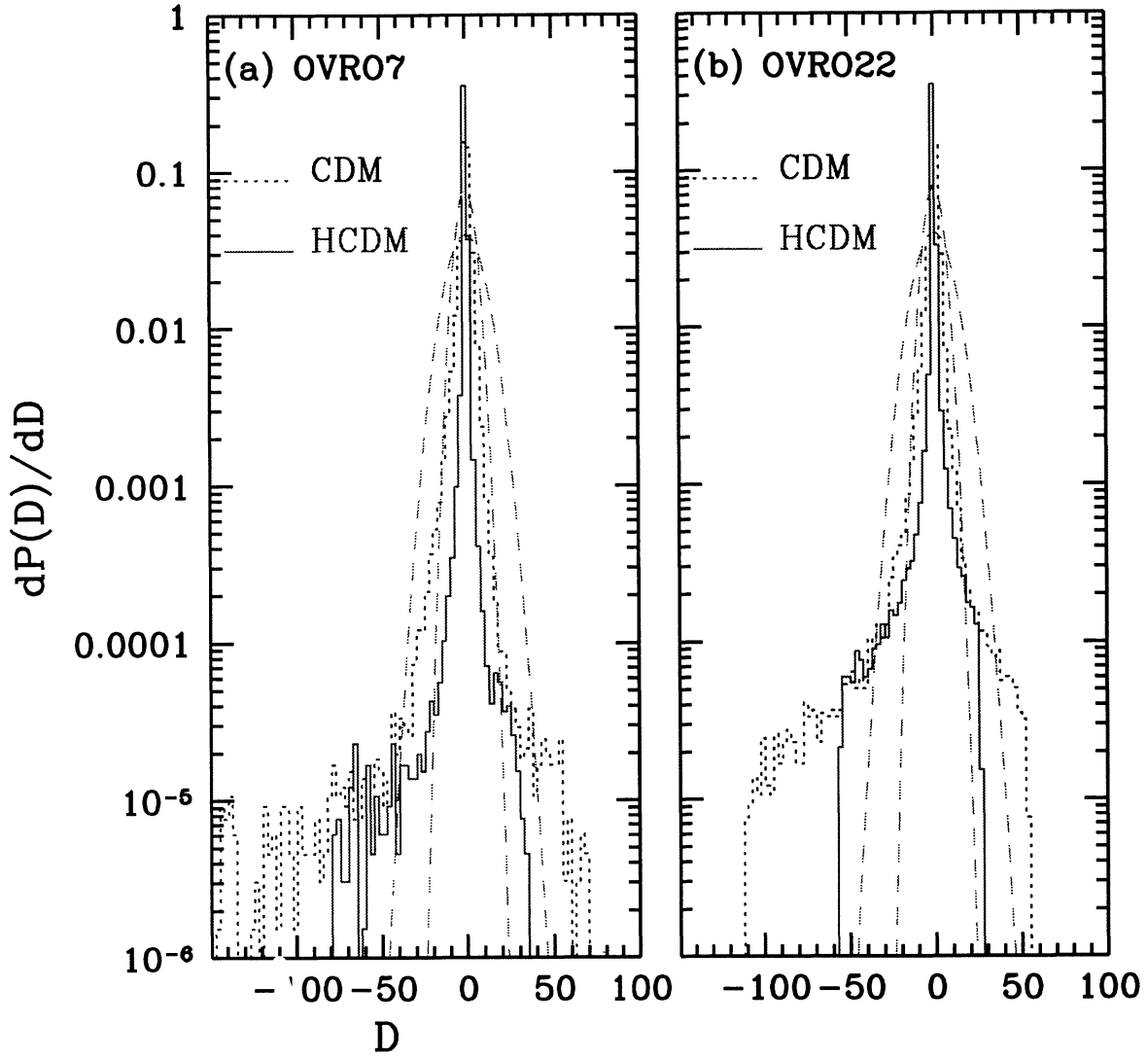

FIG. 8.—Probability distribution functions for $D \equiv 10^6 \Delta T/T$ for a three-beam experimental configuration with (*a*) OVRO parameters (FWHM of 1.'8 and throw of 7.'15) and (*b*) OVRO22 parameters (FWHM of 7.'4 and throw of 22.'16), derived from the 5° × 5° maps. The light lines are Gaussian noise distributions with levels of 10^{-5} and 5×10^{-6}. Although the rms values with a 3 beam strategy are quite small, rare excursions do lie well above these noise levels. Note that since extreme excursions with the 1.'8 beam smooth into many large excursions for the 7.'4 beam, experiments such as OVRO22 will be more effective than OVRO for searching for the ambient SZ effect. The histograms from which this figure derived had 512^2 pixels and width of 2.3 in D.

and hence smaller, and would need to be extracted from the background of primary CMB fluctuations.

One such instrument, the Cosmic Background Imager (CBI), is an interferometric array of meter-sized dishes. Plans currently envision a 5–10 element interferometer to map scales from ~2′–20′, with optimal sensitivity $\gtrsim 5'$, using HEMTs to cover frequencies 32–40 GHz, and with additional plans for a 15 GHz channel to help identify and possibly remove contamination by galactic synchrotron and free-free emission.

Figure 10 consists of 4 square-degree simulated fields that could be probed by the CBI or similar instrument: Figure 10*a* shows the SZ effect for 30 GHz; Figure 10*b*, the associated *ROSAT* map (0.1–2.4 keV), with a minimum contour level similar to the *ROSAT* 5 σ sensitivity for long exposure pointed observations; Figure 10*c*, the Thomson scattering anisotropy induced by the bulk motion of the clusters; and Figure 10*d*, primary anisotropies. The hills and valleys shown in Figure 10*d* are natural (not beam-smoothed), and mapping them will give a direct probe of the physics of how the photon decoupling region at a redshift of ~1000 damped the primary signal.

The SZ effect maps of Figure 10 have the following minima, maxima, mean offsets, and rms, in units of 10^{-6}: (Fig. 10*a*) $(-47, 0, -2.0, 3.0)C_{SZ}$; (Fig. 10*c*) $(-7.57, 6.03, -0.04, 0.36)C_V$; (Fig. 10*d*) $(-53, 48, -0.06, 18)$. Thus the SZ effect is competitive with the much larger primary anisotropies expected in this model only in the cores of clusters; and the moving-cluster anisotropies are disappointingly small, even when nonlinear corrections are included. The *ROSAT* image in Figure 10*b* has minima, maxima, mean offset of $(0, 12, 0, -0.05, 0.23) \times 10^{-14} C_X$ in intensity. Using the information in a deep field cluster catalog such as Figure 10*b* will clearly be invaluable for separating SZ from primary. Even so, since the true

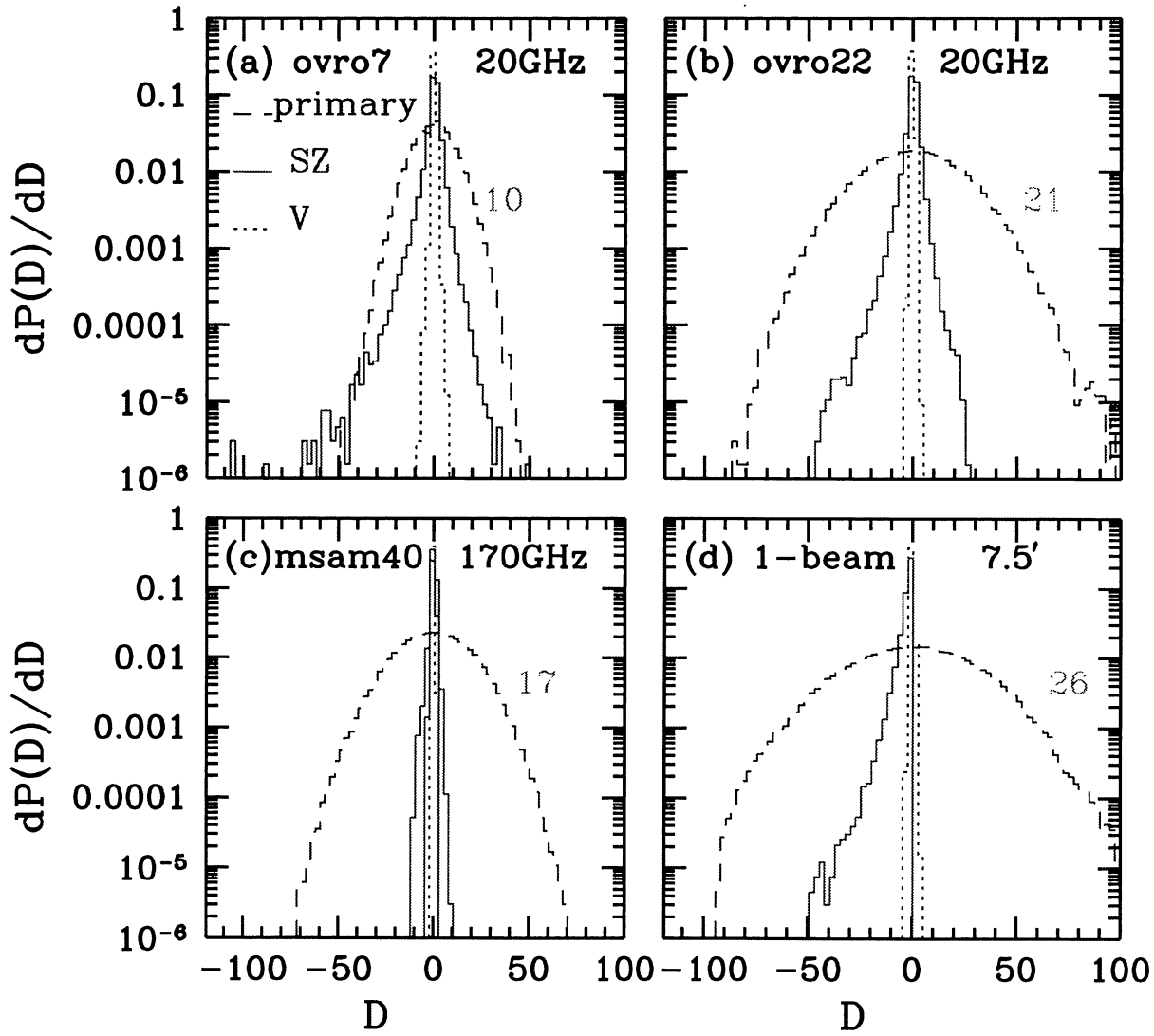

FIG. 9.—A comparison of the probability distribution functions for excursions $D \equiv 10^6\,\Delta T/T$ in smoothed 16° × 16° maps for the SZ effect at 20 GHz, the cluster velocity effect and primary anisotropies. The SZ and velocity effects are for a scale invariant CDM model with $\sigma_8 = 0.7$, which gives about the right cluster abundance. We have taken $\Omega_{B\mathrm{eff}} = 0.1$ and used a 1.2 correction on temperature for the SZ effect and a 1.2 correction on velocity for the moving cluster effect. The primary anisotropies correspond to a $\sigma_8 = 1$ (*COBE* normalized) $\Omega_B = 0.05$ CDM model, but the results scale with $\sigma_8 = 1$. The σ_8 parameters were chosen so that the probability distributions will roughly correspond to what a nearly scale-invariant HCDM model would give. The experimental configurations were three-beam experiments: (*a*) OVRO7 parameters (FWHM of 1.'8 and throw of 7.'15), (*b*) OVRO22 parameters (FWHM of 7.'4 and throw of 22.'16), (*c*) MSAM parameters (FWHM of 28′ and throw of 40′). For the MSAM configuration, the SZ effect at 170 GHz (where it is $\sim\frac{1}{3}$ of the value) is also shown. (*d*) gives the excursions with a 7.'5 beam but no switching, corresponding to what one might get from a mapping experiment (the power has been truncated beyond the fundamental mode of the patch, however). The numbers beside the primary histograms are Gaussian rms amplitudes which, of course, fit the primary distributions superbly. The histograms from which this figure derived had 512^2 pixels and width of 2.3 in D.

sky will be the sum of Figures 10*a*, 10*c*, and 10*d*—plus Galactic and extragalactic synchrotron and bremsstrahlung sources for CBI, and dust (possibly cold) for higher frequency millimeter and submillimeter—separation will not be easy especially without many widely spaced frequency bands (e.g., Brandt et al. 1994).

COBRAS/SAMBA and FIRE are satellite experiments proposed to ESA and NASA to map the entire sky using bolometers, with angular sensitivity to modes in the range $\gtrsim$ 5′–10′. With bolometers, one can straddle the frequency where the SZ effect changes sign, providing a valuable discriminator of SZ from primary $\Delta T/T$.

In Bond & Myers (1991), we concluded that the confusion from discrete nonthermal extragalactic radio sources is sufficiently severe that, unless they can be removed accurately, a successful detection of the ambient SZ effect from unidentified groups and clusters is unlikely at Rayleigh-Jeans frequencies. Experiments at millimeter and submillimeter wavelengths are likely to provide better prospects for observation of the ambient SZ effect, although there will be confusing dusty sources.

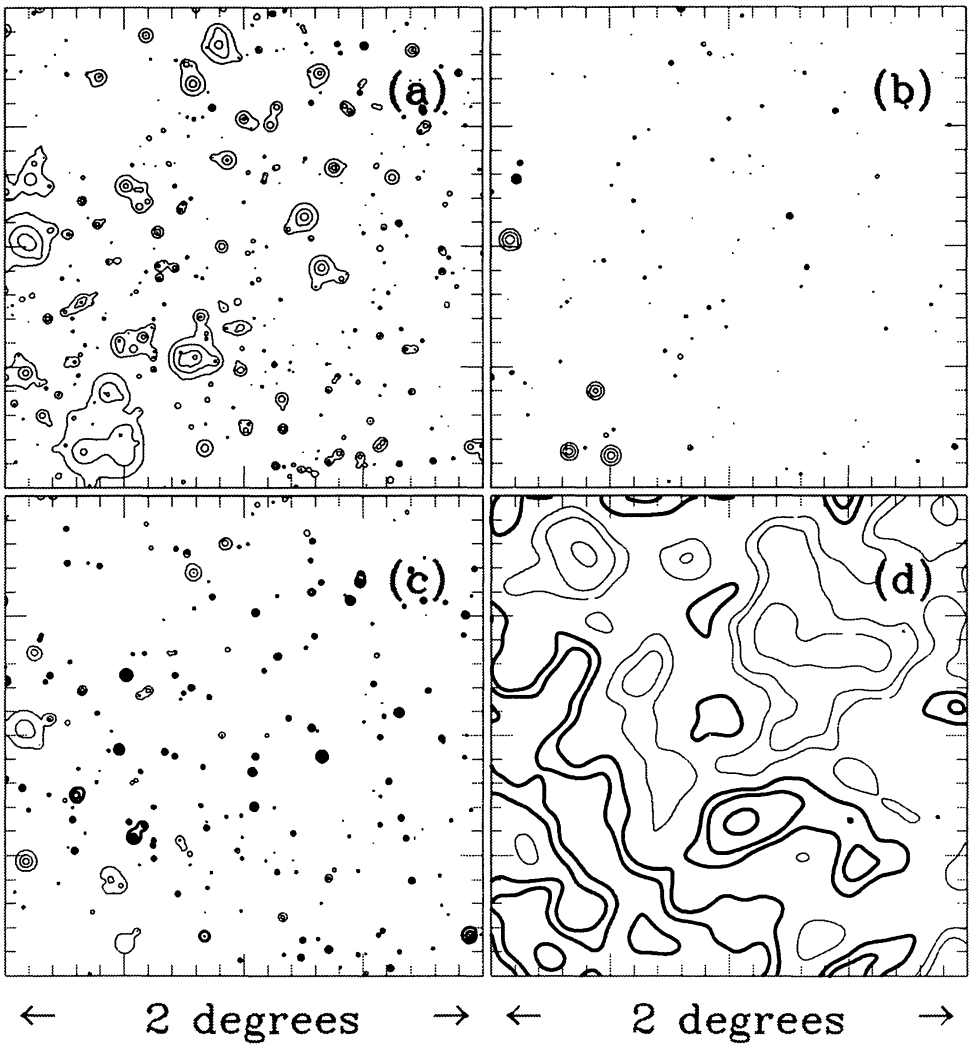

FIG. 10.—(*a–d*) Typical $2° \times 2°$ $\Delta T/T$ and X-ray maps with 500^2 pixels for a $\Omega_B = 0.05$ scale-invariant CDM model with $\sigma_8 = 0.7$: (*a*) the SZ effect for 30 GHz, with contours $-5 \times 10^{-6} C_{SZ} \times 2^{n-1}$; (*b*) the associated *ROSAT* map (0.1–2.4 keV), with contours $10^{-14} C_X \times 2^{n-1}$ ergs cm^{-1} S^{-1}; (*c*) the Thomson scattering anisotropy induced by the bulk motion of the clusters, with contours now $\pm 1.25 \times 10^{-6} C_V \times 2^{n-1}$; (*d*) primary anisotropies, with contour levels at $\pm 10 \times 10^{-6} \times 2^{n-1}$. These would be increased by a factor of 1.7 if it were *COBE* normalized. Positive contours are heavy, negative contours are light. The C_{SZ}, C_X and $C_V \approx C_{SZ}$ are order-unity correction factors. A quadratic nonlinear correction factor for the displacement has been used in (*a*, *b*, *c*) and for the bulk velocity in (*c*).

Rather more remarkable is that the primary anisotropies of the background radiation would also exceed the ambient SZ effect, given the observed *COBE* level for large angle anisotropies. However, multifrequency observations should be able to eventually disentangle the different components. Nonetheless, what is clear from our results is that creating cluster catalogues from SZ sources identified in microwave background maps will not be an easy task. What is highly worthwhile, however, will be sensitive SZ measurements following up optical or X-ray identifications of the clusters. These are now becoming feasible to faint ($\Delta T/T \sim 10^{-5}$) levels and give us the line-of-sight integrals of the gas pressure. The mean gas pressure is probably a better probe of mean cluster properties than the core-dominated X-ray emission or the possibly-biased galaxy velocity dispersion.

6. DISCUSSION AND CONCLUSIONS

There are many applications of the peak-patch picture. Peak theory has been applied to the Lyman-alpha cloud system (Bond, Szalay, & Silk 1988), "Great Attractors" and giant "cluster-patches;" Bond (1989a), the galaxy and group distribution (Bond 1989b), quasars (Efstathiou & Rees 1988), dusty protogalaxies (Bond, Carr, & Hogan 1991), etc. We have applied our method to make submillimeter and millimeter maps of the sky from starburst protogalaxies at high redshift (Bond & Myers 1993a). Using peaks for clusters began with BBKS, was applied to cluster-galaxy and cluster-cluster alignments in Bond (1986, 1987) and Bardeen, Bond, & Efstathiou (1987), and was extended to Sunyaev-Zeldovich calculations by Bond (1988) and our hierarchical peak applications (Bond

& Myers 1991, 1993b). It is the application to clusters, with special attention paid to the uncertainties, that we have focused on in this paper. The gas and temperature profiles about those peaks that survive in the catalog are currently put in by hand—albeit motivated by observed profiles—with the gross peak-patch parameters we measure such as internal energy used to scale the profiles. The large effort currently underway to accurately model clusters with three-dimensional hydrodynamical simulations should decrease this reliance on observational calibration of the final-state peak-patch properties. In § 5, we used our catalogs to construct *ROSAT* X-ray and Sunyaev-Zeldovich maps, and discussed the implications of the SZ maps for CMB anisotropy experiments at currently achievable sensitivity levels, which emphasized the strong role that SZ measurements can make in the near future in probing the cluster system.

The various maps we have constructed dramatically illustrate that what these experimental probes will see is extremely sensitive to the biasing factor for fixed values of the other physical parameters such as core radius and Ω_{Beff}. For $\Omega_{nr} = 1$ Einstein–de Sitter models, we conclude that the amplitude parameter σ_8 that best fits the data is around 0.7. Lower values, down to 0.6, can fit the Edge et al. (1990) temperature distribution, and, provided the power spectrum is appropriately flattened, can even accomodate a 14 keV cluster at $z \approx 0.2$ found by Arnaud et al. (1992) with the *Ginga* satellite. It is also clear that σ_8 above 0.9 overproduces high velocity dispersion clusters. We therefore remain comfortable with our original estimation of 0.65–0.9 given in Bond & Myers (1991) using an earlier version of the peak-patch approach. Adopting the higher kinetic velocities to normalize temperature makes the range 0.6–0.8 more plausible. We also emphasize that because flatter spectra are desired, one's estimate of the spectrum amplitude depends upon which range of cluster data one is trying to fit. We are most interested in the rare event side, which is extremely sensitive to spectral changes.

This research was supported by the NSERC of Canada at CITA and by the NSF at Caltech. JRB was supported by a Canadian Institute for Advanced Research Fellowship.

REFERENCES

Adams, F. C., Bond, J. R., Freese, K., Frieman, J. A., & Olinto, A. V. 1993, Phys. Rev. D, 47, 426
Arnaud, K., Hughes, J. P., Forman, W., Jones, C., Lachieze-Rey, M., Yamashita, K., & Hatsukade, I. 1992, ApJ, 390, 345
Babul, A., & Katz, N. 1993, ApJ, 406, L51
Bahcall, N., & Cen, R. 1993, ApJ, 407, L49
Bardeen, J. M., Bond, J. R., & Efstathiou, G. 1987, ApJ, 321, 28
Bardeen, J. M., Bond, J. R., Kaiser, N., & Szalay, A. S. 1986, ApJ, 304, 15 (BBKS)
Bardeen, J., Steinhardt, P., & Turner, M. S. 1983, Phys. Rev. D, 28, 679
Bartlett, J. G., & Silk, J. 1993, ApJ, 407, L45
Birkinshaw, M. 1990, in The Cosmic Microwave Background: 25 Years Later, ed. N. Mandolesi & N. Vittorio (Dordrecht: Kluwer), 77
Birkinshaw, M., Hughes, J. P., & Arnaud, K. A. 1991, ApJ, 379, 466
Blanchard, A., Wachter, K., Evrard, A. E., & Silk, J. 1992, ApJ, 225, 505
Bond, J. R. 1986, in Galaxy Distances & Deviations from the Universal Expansion, ed. B. F. Madore & R. B. Tully (Dordrecht: Reidel), 255
———. 1987, in Nearly Normal Galaxies From the Planck Era to the Present, ed, S. Faber (New York: Springer), 388
———. 1995, Phys. Rev. Lett., 74, 4369
———. 1988, in Proc. NATO Summer School, The Early Universe, 1986 Aug. ed. W. G. Unruh (Dordrecht: Reidel), 283
———. 1989a, in Proc. Vatican Study Week, Large-Scale Motions in the Universe, ed. V. Rubin, & G. Coyne (Princeton: Princeton Univ. Press), 419
———. 1989b, in Frontiers of Physics - From Colliders to Cosmology, ed. A. Astbury et al. (Singapore: World Scientific), 182
Bond, J. R., Carr, B. J., & Hogan, C. J. 1991a, ApJ, 367, 420
Bond, J. R., Centrella, J., Szalay, A. S., & Wilson, J. R. 1984, MNRAS, 210, 515
Bond, J. R., Cole, S., Efstathiou, G., & Kaiser, N. 1991b, ApJ, 379, 440
Bond, J. R., Crittenden, R., Davis, R., Efstathiou, G., & Steinhardt, P. 1994, Phys. Rev. Lett. 72, 13
Bond, J. R., & Efstathiou, G. 1991, Physics Letters B, 379, 440
Bond, J. R., & Myers, S. 1991, Trends in Astroparticle Physics, D. Cline & R. Peccei, Singapore: World Scientific, 262
———. 1993a, in Proc. 3d Teton Summer School, The Evolution of Galaxies and Their Environment, ed. M. Shull & H. Thronson, NASA Conf. Publ. 3190, 21
———. 1993b, in Proc. Teton Summer School, The Evolution of Galaxies and Their Environment, ed. M. Shull & H. Thronson, NASA Conf. Publ. 3190, 52
———. 1995a, ApJS, 103, 1 (BM1)
———. 1995b, ApJS, 103, 41 (BM2)
———. 1995c, preprint (BM4)
Bond, J. R., Szalay, A. S., & Silk, J. 1988, ApJ, 324, 627
Brainerd, T. G., & Villumsen, J. V. 1992, ApJ, 394, 409
Brandt, W. N., Lawrence, C. R., Readhead, A. C. S., Pakianathan, J. N., & Fiola, T. M. 1994, ApJ, 424, 1
Carlberg, R. G., & Couchman, H. M. P. 1989, ApJ, 340, 47
Carlberg, R. G., & Dubinski, J. 1991, ApJ, 369, 13
Carlberg, R. G., et al. 1993, JRASC, 88, 39
Carlstrom, J. E., Joy, M., & Greggo, L. 1995,
Cen, R., & Ostriker, J. P. 1992, ApJ, 393, 22
Cheng, E. S., et al. 1994, ApJ, 422, L37
Cole, S., & Kaiser, S. 1988, MNRAS, 233, 637
Couchman, H. M. P., & Carlberg, R. G. 1992, ApJ, 389, 453
Davis, M., Summers, F. J., & Schlegel, D. 1992, Nature, 359, 393
Dubinski, J., & Carlberg, R. G. 1991, ApJ, 378, 496
Edge, A. C., & Stewart, G. C. 1991, MNRAS, 252, 428
Edge, A. C., Stewart, G. C., Fabian, A. C., & Arnaud, K. A. 1990, MNRAS, 245, 559
Efstathiou, G., Bond, J. R., & White, S. D. M. 1992, MNRAS, 258, 1P
Efstathiou, G., Frenk, C. S., White, S. D. M., & Davis, M. 1988, MNRAS, 235, 715
Efstathiou, G., & Rees, M. 1988, MNRAS, 230, 5P
Evrard, G. 1990a, ApJ, 363, 349
———. 1990b, in Clusters of Galaxies, W. R. Oegerle, M. Fitchett, & L. Danly (Cambridge: Cambridge Univ. Press), 287
Evrard, G., & Henry, P. 1991, ApJ, 383, 95
Frenk, C. S., White, S. D. M., Efstathiou, G., & Davis, M. 1990, ApJ, 351, 10
Gaier, T., Schuster, J., Gunderson, J., Koch, T., Seiffert, M., Meinhold, P., & Lubin, P. 1992, ApJ, 398, L1
Gioia, I. M., Henry, J. P., Maccacaro, T., Morris, S. L., Stocke, J. T., & Wolter, A. 1990, ApJ, 356, L35
Grainge, K., et al. 1994, MNRAS, 265, L57
Gunderson, J., et al. 1993, ApJ, 413, L1
Henry, J. P., & Arnaud, K. A. 1991, ApJ, 372, 410
Henry, J. P., Gioia, I. M., Maccacaro, T., Morris, S. L., Stocke, J. T., & Wolter, A. 1992, ApJ, 386, 408
Herbig, T., Lawrence, C. R., Readhead, A. C. S., & Gulkis, S. 1995, ApJ, 449, L5
Hernquist, L. 1990, ApJ, 356, 359
Hughes, J. P. 1989, ApJ, 337, 21

Jones, M., et al. 1993, Nature, 365, 320
Kaiser, N. 1991, ApJ, 383, 104
Klypin, A., Holtzman, J., Primack, J., & Regos, E. 1993, ApJ, 416, 1
Meinhold, P. 1993, ApJ, 409, L1
Merritt, D. 1987, ApJ, 313, 121
Mushotzky, R. 1988, in Hot Thin Plasmas in Astrophysics, ed. R. Pallavicini (Dordrecht: Kluwer), xxx
———. 1993, in Proc. 16th Texas Symp. on Relativistic Astrophysics, ed. C. Akerlof & M. Srednicki (New York: New York Acad. Sci.), xxx
Myers, S. T., Readhead, A. C. S., & Lawrence, C. R. 1993, ApJ, 405, 8
Narayan, R., & White, S. D. M. 1987, MNRAS, 231, 97P
Oukbir, J., & Blanchard, A. 1992, A&A, 262, L21 225, 505
Peebles, P. J. E., Daly, R. A., & Juszkiewicz, R. 1989, ApJ, 347, 563
Readhead, A. C. S., et al. 1989, ApJ, 346, 556
Salopek, D. S., Bond, J. R., & Bardeen, J. M. 1989, Phys. Rev. D, 40, 1753
Sarazin, C. 1986, Rev. Mod. Phys., 58, 1
Smoot, G., et al. 1992, ApJ, 396, L1
Sunyaev, R. A., & Zeldovich, Ya. B. 1980, ARA&A, 18, 537
The, T., & White, S. D. M. 1986, AJ, 92, 1248
van Dalen, A., & Schaeffer, R. K. 1992, ApJ, 398, 33
Walker, T. P., Steigman, G., Schramm, D. N., Olive, K. A., & Kang, H. S. 1991, ApJ, 376, 51
White, S. D. M., Briel, U. G., & Henry, J. P. 1993, MNRAS, 261, P8
White, S. D. M., Efstathiou, G., & Frenk, C. S. 1993, MNRAS 262, 1023
Wilbanks, J., et al. 1994, ApJ, 427, L75
Wright, E., et al. 1994, ApJ, 420, 1